

Airflow measurements at a wavy air–water interface using PIV and LIF

Marc P. Buckley¹  · Fabrice Veron²

Received: 12 December 2016 / Revised: 9 September 2017 / Accepted: 11 September 2017
© The Author(s) 2017. This article is an open access publication

Abstract Physical phenomena at an air–water interface are of interest in a variety of flows with both industrial and natural/environmental applications. In this paper, we present novel experimental techniques incorporating a multi-camera multi-laser instrumentation in a combined particle image velocimetry and laser-induced fluorescence system. The system yields accurate surface detection thus enabling velocity measurements to be performed very close to the interface. In the application presented here, we show results from a laboratory study of the turbulent airflow over wind driven surface waves. Accurate detection of the wavy air–water interface further yields a curvilinear coordinate system that grants practical and easy implementation of ensemble and phase averaging routines. In turn, these averaging techniques allow for the separation of mean, surface wave coherent, and turbulent velocity fields. In this paper, we describe the instrumentation and techniques and show several data products obtained on the air-side of a wavy air–water interface.

1 Introduction

The physical processes at a gas–liquid interface are important for many industrial applications as well as natural environmental problems. In the engineering sector, coupled interfacial gas–liquid dynamics are of interest because they influence the efficiency of chemical reactors, boilers, turbines (Turney and Banerjee 2008; Hewitt 2013). In the

geophysical sphere, which largely motivates this study, fluxes of momentum and scalars across the wavy air–sea interface provide boundary conditions for both the atmosphere and the oceans and are therefore, pivotal in controlling the evolution of weather and climate. These fluxes are affected by fine-scale, coupled dynamics above and below the wavy ocean surface. In fact, the surface waves significantly modify the boundary layers on both sides of the interface and it is now well established that it is through wave-related dynamical processes that the air and water boundary layers are coupled (see Sullivan and McWilliams (2010) for a review on the topic).

On the water side, for example, it has been shown that the interaction between the wave-induced Lagrangian mass transport, i.e. the Stokes drift, and the surface shear current, leads to the generation of Langmuir circulations, causing significant mixing of the water column (Skylvingstad and Denbo 1995; McWilliams et al. 1997; Noh et al. 2005; Li et al. 2005; Harcourt and D’Asaro 2008; Grant and E 2009; Veron et al. 2009; Kukulka et al. 2010; Belcher et al. 2012; D’Asaro 2014). When surface waves break, the turbulence injected into the water column also significantly enhances surface mixing (Drennan et al. 1996; Melville et al. 1998; Veron and Melville 1999; Melville et al. 2002; Thorpe et al. 2003; Gemmrich and Farmer 2004) and leads to substantial deviations from the classical theories (Agrawal et al. 1992; Thorpe 1993; Melville 1994; Anis and Moum 1995; Melville 1996; Terray et al. 1996; Veron and Melville 2001) and causes significant energy dissipation (Banner et al. 2014; Thomson et al. 2016; Schwendeman et al. 2014; Zappa et al. 2016; Sutherland and Melville 2013, 2015).

On the air side, it is clear that surface wave processes also play an important role in the kinematics and dynamics of the boundary layer (e.g. Janssen 1989; Komen et al. 1994; Belcher and Hunt 1998; Hristov et al. 1998; Edson

✉ Marc P. Buckley
mbuckley@udel.edu

¹ Helmholtz Zentrum Geesthacht, 21502 Geesthacht, Germany

² University of Delaware, Newark, DE 19716, USA

and Fairall 1998; Janssen 1999; Sullivan and McWilliams 2002; Sullivan et al. 2008; Yang and Shen 2010; Suzuki et al. 2013; Grare et al. 2013a; Hara and Sullivan 2015). Airflow separation for example, is the kinematic air-side equivalent to wave breaking in the water (Banner and Melville 1976; Gent and Taylor 1977), a process which is known to generate turbulence and enhance dissipation (Rapp and Melville 1990; Melville et al. 2002; Drazen and Melville 2009). Thus, airflow separation is similarly expected to dramatically affect the structure of the wind stress (drag) upon the ocean surface (Banner and Melville 1976; Buckley and Veron 2016). In fact, recent measurements and models of drag at the ocean surface at moderate to high wind speeds suggest that a large fraction of the momentum transfer at the surface is supported by the short gravity-capillary wind waves (Kudryavtsev and Makin 2001, 2002; Donelan et al. 2004; Mueller and Veron 2009). The presence of waves also reduces the turbulent fraction of the stress near the surface, within the so-called wave boundary layer (WBL). Therefore, within the atmospheric boundary layer, the local turbulent stress changes with height above the surface, producing inhomogeneity in both the horizontal and vertical directions (Janssen 1989, 1999; Belcher and Hunt 1993; Komen et al. 1994; Hare et al. 1997; Edson and Fairall 1998). Thus, the presence of the surface waves causes the surface stress to become a function of the sea state.

In spite of a large body of existing literature on the topic of wind-wave interactions, it remains difficult to quantify the influence of wave-coherent effects on air–sea momentum and energy fluxes, and to distinguish them from turbulent contributions. (Lumley and Terray 1983; Thais and Magnaudet 1996; Hristov et al. 1998; Veron et al. 2008; Grare et al. 2013a). This is in part due to the technical difficulty associated with making measurements close to the air water interface in the laboratory or the field, and the difficulty in modeling the complex non-linear interactions between the turbulence and the surface waves. On the water side, Peirson (1997) developed a particle image velocimetry system (PIV) capable of measuring the details of the boundary layer beneath laboratory wind waves, and particularly the viscous stress just below the water surface (see also Banner and Peirson 1998). Later, Siddiqui and Loewen (2010) were able to estimate phase-averaged turbulent quantities below short laboratory wind waves, by combining an underwater PIV camera with an air-side surface-detection camera. However, their limited field of view made it difficult to obtain meaningful, converging estimates of near-surface phase-averaged quantities. On the air side, Reul et al. (1999) were the first to obtain 2D PIV velocity fields in the air over mechanically generated breaking waves, showing detailed vortical structures of airflow separating past wave crests. Later, Veron et al. (2007) were able to estimate viscous stresses in the air above wind-generated waves by PIV. Grare (2009) and

Grare et al. (2013b) obtained single point airflow velocity measurements above laboratory wind waves, by repeatedly plunging a hot wire anemometer into the water for each experimental condition. Using this innovative method, they measured vertical airflow velocity profiles with 1 velocity measurement every 50 μm , and computed viscous and form drags above wind waves (Grare et al. 2013b). However, due to the one-dimensionality of their measurement system, wave phase detection was only indirectly achieved using a single point wave gauge (Grare 2009); additionally the instantaneous spatial along-wave structure of the airflow was not resolved. Recently, Buckley and Veron (2016), using the combined PIV-LIF experimental system described herein, were able to characterize, as a function of wave age, the instantaneous fine-scale structure of the airflow above wind and mechanically generated waves, in low to moderate wind speeds. Using phase and wave profile information, they extracted turbulent velocity fields over thousands of waves, derived meaningful phase-averaged airflow characteristics, and showed the influence of wave age on the phase-averaged wave-coherent and turbulent quantities in the airflow.

In this paper, we describe the technical details of the experimental setup used in Buckley and Veron (2016), which was specifically developed for the measurement and study of the turbulent airflow above a moving wavy water surface, from low to high wind speeds. Here, we specifically focus on the instrumentation, techniques, and analysis methods. We also provide examples of advanced data products obtained using this system, including physically relevant invariants of the velocity gradient tensor (e.g., swirling strength) and phase-averaged turbulent quantities. The remaining of the paper is organized as follows: in Sect. 2, we present the details of the experimental setup and methods developed for this study. In Sect. 3, we present results from our airflow measurements as well as examples of data products that can then be readily obtained from the data. Finally, we offer a brief conclusion in Sect. 4.

2 Experimental methods

A complex experimental system was developed, to simultaneously measure along-wind wave elevation profiles and two-dimensional velocities in the airflow within the first 10 cm above waves and as close as 0.1 mm from the water surface. The main objectives of the experimental apparatus were to:

- Combine Laser-induced fluorescence (LIF) surface detection and Particle image velocimetry (PIV) to measure velocities and velocity gradients as close as possible to the air–water interface in the presence of wind and wind-generated waves.

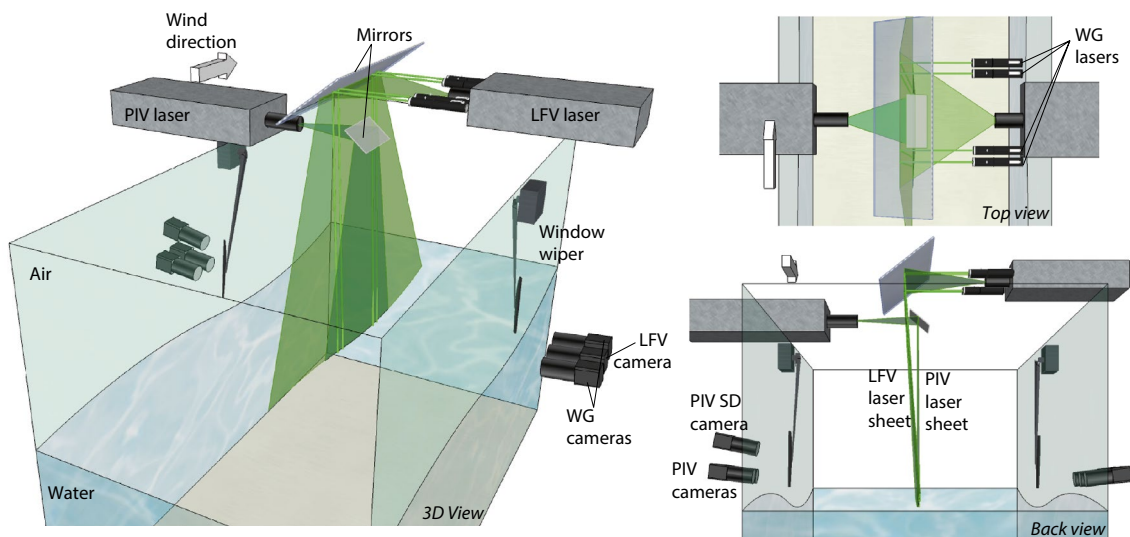


Fig. 1 Sketch of the wind and wave imaging system positioned at a fetch of 22.7 m. The setup is shown from three different points of view (3D, top, and back views). The airflow velocity measurement system is on the right of the tank. It comprises a combination of particle image velocimetry (PIV, velocity measurements) and laser-induced fluorescence (PIVSD, surface detection on the PIV images). Both make use of the PIV laser sheet for illumination. The PIV uses

direct laser light scattered by freshwater fog droplets; the PIVSD uses fluorescence of the rhodamine 6G present in the water. The wave field measurement system is on the left of the tank, and consists of a large field of view spatial wave profile imager (LFV), and four single point laser wave gauge systems (WG). Both LFV and WG are using laser-induced fluorescence

- Use large field of view LIF to measure the wave field within regions upwind and downwind of the airflow PIV measurement area, and apply Fourier analysis to the detected surface profiles to define a meaningful surface-following coordinate system and determine wind wave phases.
- Utilize both the surface-following coordinate system and wave phases to perform ensemble and phase averaging to extract mean, wave-coherent, and turbulent velocity fields, from the instantaneous velocity measurements.

2.1 Experimental setup and instrumentation

The experiments presented here were conducted in the large wind-wave-current tank at the Air Sea Interaction Laboratory of the University of Delaware, in Lewes, Delaware. The facility is specifically designed and equipped for studies in air–sea interactions. The tank is 42 m long, 1 m wide and 1.25 m high. During the experiments described in this study, the water depth was kept at 0.70 m. An artificial permeable wave-absorbing beach was placed at the downwind end of the tank to dissipate wave energy and eliminate wave reflections. The tank is equipped with a programmable, computer-controlled, recirculating wind tunnel, with a honeycomb flow straightener used to condition the airflow before it reaches the test section of the tank. The main test section where the waves and airflow were measured was placed at a

fetch of 22.7 m, where fetch is defined as the distance from the point where the wind tunnel reaches the water, to the center of the PIV imaging area.

A complex imaging system, using a combination of PIV and LIF techniques, was specifically developed for this study. As a result, we were able to measure velocities in the air above waves, on average as close as 0.1 mm above the air–water interface. In addition to wind velocities, temporal and spatial wave properties were measured by LIF, simultaneously with the velocity measurements. A three-dimensional sketch of the instrument setup is presented in Fig. 1. The specifications of all imaging devices are listed in Table 1 and additional details are provided in the following sections.

2.2 Particle image velocimetry measurements of the airflow above waves

We developed a PIV system, capable of measuring along-channel 2D velocity fields in the air above wind waves. For this, the airflow was seeded with 8–12 μm water droplets generated by a commercial freshwater fog generator (Micro-cool Inc.) equipped with 28 fog nozzles, affixed to the airflow straightener at the location of zero fetch. Freshwater seeding particles were employed to avoid any influence on the surface tension of the (freshwater) waves. In the PIV technique, small particles seed the flow and act as near Lagrangian tracers that are then illuminated with a flashed light source and

Table 1 Specifications of the imaging devices

Camera name	PIV (#1)	PIV (#2)	PIVSD	LFV	WG1	WG2
Technique	PIV	PIV	LIF	LIF	LIF	LIF
Model	TM-4200	TM-4200	TM-4200	TM-4200	CV-M2	CV-M2
CCD (pixel × pixel)	2048 × 2048	2048 × 2048	2048 × 2048	2048 × 2048	300 × 1600	300 × 1600
Resolution (μm/pixel)	47	47	100	250	66	66
FOV (cm × cm)	9.63 × 9.63	9.63 × 9.63	20.48 × 20.48	51.20 × 51.20	1.98 × 10.56	1.98 × 10.56
FPS	14.4	14.4	14.4	7.2	93.6	93.6
Lens focal length (mm)	105	105	50	14	60	60
Amber filter	No	No	Yes	Yes	Yes	Yes
Data type	Velocities	Velocities	$\eta(x)$	$\eta(x)$	$\eta_1(t), \eta_2(t)$	$\eta_3(t), \eta_4(t)$
NOF	115,314	115,314	115,314	57,657	749,541	749,541

The following abbreviations are used in the table below: *CCD* charged coupled device, *FOV* field of view, *FPS* frames per second, $\eta(x)$ along-channel instantaneous surface profile, $\eta_i(t)$ single-point surface elevation time series, *NOF* number of frames acquired

imaged with a digital camera. The motion of the particles between two flashes then yields a local velocity estimate. Here, the Stokes time scale of the particles is $\tau_p = 0.3$ ms (e.g., Raffel et al. 2013). At the lowest wind speed, τ_p is 130 times smaller than the Kolmogorov time scale τ_k (estimated in the bulk flow at the height of a wavelength, and using the measured friction velocity—Table 2). At the highest wind speed, τ_p is at least five times smaller than τ_k . Given these Stokes numbers $S_t = \tau_p/\tau_k$, the seeding particles are anticipated to accurately follow the turbulent fluid motions in all conditions presented, with an accuracy of order 1% or better (Tropea et al. 2007). Furthermore, using the transfer function of tracing particles in a turbulent flow (i.e. the particle response) from Mei (1996), and a representative turbulent energy spectrum of the form $E(\omega) \propto \omega^{-5/3}$ (e.g., Kaimal and Finnigan 1994; Li et al. 2015), we estimate that more than 99% of the fluid's velocity variance is resolved from the tracer particle motion, for all wind speeds studied.

The particles were illuminated by a high intensity green laser sheet generated by a pulsed dual-head Nd–Yag laser system (New Wave Research, 200 mJ/pulse, 3–5 ns pulse duration, 532 nm wavelength), fitted with a set of cylindrical and spherical lenses. It should be noted that each Nd–Yag laser system is actually composed of two pulsed lasers. The output beams of both internal lasers are internally routed and aligned such that their optical paths are identical, once outside the laser head. Each laser can flash at a frequency of up to 15 Hz. The two lasers can be flashed simultaneously, or with a time delay Δt . For PIV, Δt is generally adjusted such that particle displacements are optimal on the PIV images. This time delay depends on the flow velocity and the size of the image detected (Raffel et al. 2013). In this study, the adjustable laser sheet thickness was set to approximately 0.3 cm, to provide crisp, in focus, high resolution images of the PIV particles (see the example image in panel a of Fig. 2 below).

The particles illuminated by the green flashed laser were imaged by two side-by-side CCD cameras (Jai TM4200CL, 2048 × 2048 pixels) (see Fig. 1). Each of these PIV cameras was fitted with a 105 mm telephoto lens (Nikon). The adjacent PIV frames were collated to obtain a single high resolution (47 μm/ pixel) 18.7 × 9.6 cm PIV image. The PIV cameras operated at 14.4 frames/second yielding velocity fields at a 7.2 Hz rate. To minimize direct high intensity laser light reflections from the wavy water surface into the PIV cameras, the PIV laser sheet was slightly tilted, with an angle $\leq 3^\circ$ with respect to the vertical. The laser sheet tilt was kept minimal so as to assure that the measurements were all taken in the same along-wind plane. To avoid the obstruction of the imaged near-surface region by the waves or the water meniscus at the glass wall of the tank, all cameras were also slightly tilted downward by $\leq 4^\circ$. The angle of camera tilt was chosen sufficiently small such that the entire imaged plane (laser sheet plane) was still fully in focus on the images. This was possible because the depth of the cameras' field of view was made large enough ($O(1)$ cm), by properly adjusting the camera lens apertures.¹ The wall meniscus problem was encountered, for example, by Belden and Techet (2011), who also solved it by tilting their PIV cameras. Finally, it should be noted that the acquired images were corrected for both lens distortions and variations in spatial resolution due to the slight tilt.

The PIV images were processed using an algorithm based on the adaptive PIV algorithm described in Thomas et al. (2005), which relies on a pyramid cascade of increasingly smaller and shifting interrogation windows to achieve large dynamical range in the detected velocity. A central difference

¹ Cameras and laser sheets were tilted to maximize data quality, but the angles of tilt were kept to a minimum, to not compromise measurement accuracy.

Table 2 Summary of mean experimental conditions

U_{10} m s ⁻¹	u_* cm s ⁻¹	C_p m s ⁻¹	a_p cm	λ_p m	$a_p k_p$	f_p Hz
0.86	2.6	n/a	n/a	n/a	n/a	n/a
2.19	7.3	0.47	0.15	0.14	0.07	3.3
5.00	16.7	0.62	0.50	0.25	0.13	2.5
9.41	31.4	0.78	1.20	0.39	0.19	2.0
14.34	53.8	0.87	1.96	0.48	0.26	1.8
16.63	67.2	0.92	2.29	0.54	0.27	1.7

For each experiment, the friction velocity u_* and 10-m extrapolated velocity U_{10} were computed by fitting the logarithmic part of the mean PIV velocity profile in the air. Peak wave frequencies f_p were obtained from laser wave gauge frequency spectra (WG). Other parameters with subscript p were derived by applying linear wave theory to f_p . The wave amplitude a_p was obtained from root-mean-square amplitude $a_p = \sqrt{2}a_{rms}$ computed from the WG water surface elevation time series

scheme was used to compute displacements within the PIV images. The PIV images were processed with final interrogation windows of 8×8 pixel, with 50% window overlap, yielding 1 velocity vector measurement on a 2D grid with 188 μm spacing in each (horizontal and vertical) direction.

While we expect the seeding particles to accurately follow the turbulent motions in the fluid, errors in detecting the position of the particles can nonetheless lead to errors in the measured fluid velocity. Here, subpixel accuracy was obtained by means of a three-point Gaussian interpolation on the cross-correlation field obtained at the last level of the iterative PIV routine. Given the size of the particles ($\approx 2\text{--}3$ pixels), we estimate a subpixel accuracy on the order of 0.05 pixels (Raffel et al. 2013). This yields an error on the velocity of up to 4.7 cm s^{-1} (at the highest wind speed) which corresponds to 0.3% of the bulk flow velocity. The velocity error is as low as 7.8 mm s^{-1} at the lowest wind speed, corresponding to about 0.9% of the bulk flow speed. Finally, correlation is known to decrease in the presence of shear (Adrian and Westerweel 2011), particularly if the flow is not homogeneous within an interrogation window. We estimate, as we did for the Stokes time scales above, that the Kolmogorov length scale is on the order of the resolution of the PIV measurements. Thus, turbulent particle motions within a PIV interrogation window should be minimal. Nonetheless, we expect high shear near the interface (see below) and as such, only displacement estimates with a cross-correlation of more than 50% were kept. Remaining outliers, if any, were subsequently discarded.

To obtain spatial gradients of the velocities, first cubic smooth spline shells were fitted to the instantaneous velocity fields. Spatial gradients of the velocities were computed by performing an analytical derivative of the spline fits (Spedding and Rignot 1993; Fouras and Soria 1998; Cohn and Koochesfahani 2000; Kimmoun and Branger 2007). Given the errors on the velocity estimates mentioned above, we estimate that the minimum detectable shear ranges from 20 s^{-1} at the lowest wind speed to 125 s^{-1} at the highest wind

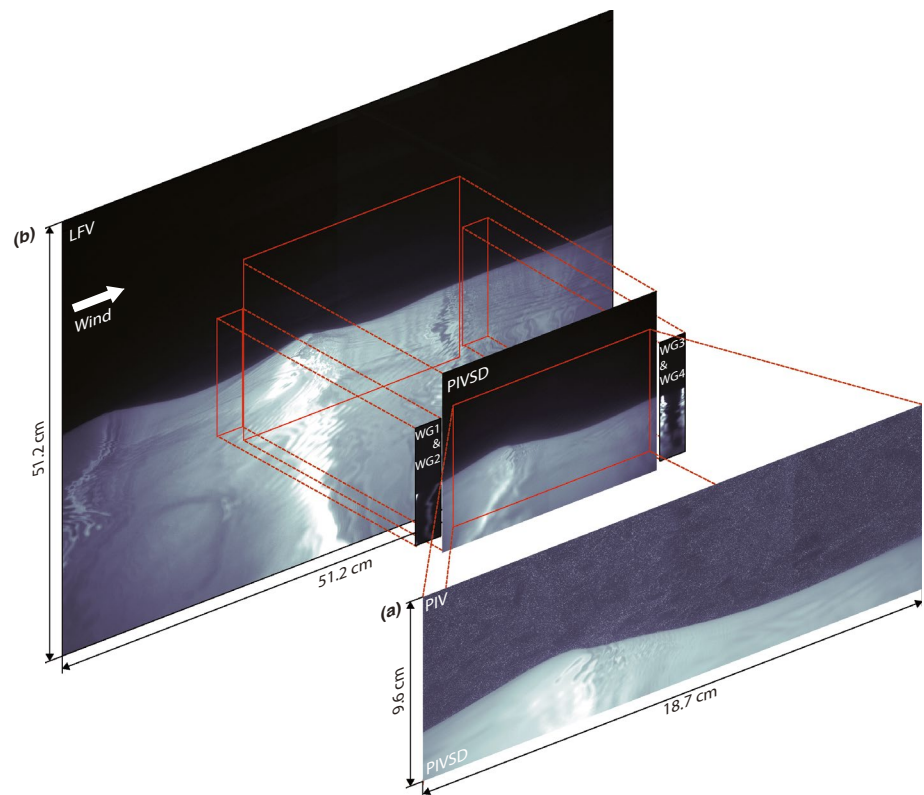
speed (Adrian 1997). Practically, this means that there is a minimum measurable stress; in these experiments this threshold is at most 6% of the total turbulent stress ρu_*^2 . At the highest wind speed, the shear near the surface is anticipated to be substantial. In these extreme conditions, we estimate that the averaging over an interrogation window inherent to the PIV technique would lead to an underestimate of the surface shear of up to 15% at the surface, within the air-side viscous sublayer.

To avoid contaminating airflow velocity calculations with the water-side portion of the image, the PIV algorithm was run only on the portion of the image that is in the air above the instantaneous water surface (André and Bardet 2014). Here, the subsurface portion of the image was entirely removed. However, locating the air–water interface (automatically) in the PIV images is difficult because the interface scatters the laser light only weakly. To address this issue, we employed a LIF technique described below.

2.3 Laser-induced fluorescence detection of the interface

To precisely and programmatically (using Matlab, Mathworks) detect the position of the interface within the thousands of acquired PIV images (see NOF values in Table 1), we acquired high resolution (100 $\mu\text{m}/\text{pixel}$) LIF images (PIV surface detection images, noted “PIVSD” hereafter) of the wave surface profiles. Previous PIV investigations of the flow below or above waves were generally challenged by the lack of high quality water surface elevation data, rendering surface detection on the PIV images difficult. The PIVSD images encompass the PIV field of view and were acquired simultaneously with the PIV images. They were acquired using another CCD camera (Jai TM4200CL, 2048×2048 pixels), and using the illumination provided by the PIV laser (Fig. 1). The PIVSD camera lens (Nikon, 50 mm) was fitted with an amber acrylic bandpass optical filter (Kentek ACRX-BB2 optical filter, with 6.1 optical density (OD)

Fig. 2 In the foreground (a), the air-side portion of the collated raw PIV image, is plotted above water-side portion of PIVSD image used for surface detection. The airflow is densely and uniformly seeded with fog particles. In the background (b), examples of laser-induced fluorescence (LIF) images are displayed, and the locations of all LIF camera fields of view are shown. Note that, since the LIF cameras are fitted with amber bandpass filters, the green-light reflecting fog particles are invisible, rendering these images ideal for automatic surface detection. All images shown here were acquired nearly at the same instant in time, with time intervals between snapshots less than $30 \mu\text{s}$. No motions of the water surface are detectable (with an image resolution of $100 \mu\text{m}/\text{pixel}$) within that time interval



at 532 nm , and $\text{OD} < 0.6$ at 566 nm). Rhodamine 6G dye (excitation at 532 nm , and maximum emission at 566 nm) was added to the water at a concentration of $8 \times 10^{-6} \text{ g L}^{-1}$. Thus, the pulsed PIV laser sheet not only illuminated the air-side PIV tracer fog particles to be imaged by the PIV cameras, but also excited the fluorescence of Rhodamine at the air–water interface, to be imaged by the LIF camera (PIVSD). Note that the amber optical filter on the PIVSD camera lens allowed the resulting PIVSD images to only show the fluorescing water (amber color), without being contaminated by light scattered from the (green) PIV fog particles (see PIVSD image in Fig. 2b). A sample stitched PIV-PIVSD image is also plotted in Fig. 2, in panel a.

In addition, automotive window wipers were placed in front of the cameras inside the flume to clean the accumulated fog off the tank windows. Special attention was given to the placement of the wipers so that they would not interfere with the imaged airflow. Finally, a rectangular piece of rubberized hog hair (generally used as filtering material in industrial HVAC systems) was placed at the bottom of the tank, under the imaging area, to scatter refracted laser light and avoid intense reflections back into the imaging area.

To locate the interface in the LIF images (PIVSD), we developed a surface (or edge) detection algorithm based on local variations of image intensity gradients, computed by kernel convolution. Using this method, the uncertainty on the location of the water surface on the PIV images was

estimated to be $\pm 0.1 \text{ mm}$. The algorithm was then applied to the PIVSD images to locate the surface. High resolution surface detection on the PIV images is necessary to accurately detect the height of our airflow PIV measurements with respect to the water surface. Since one airflow velocity vector was measured by PIV approximately every 0.2 mm , we estimate that velocity measurements closest to the water surface were achieved on average 0.1 mm above the water surface. This proximity to the surface provided velocity measurements within the viscous layer in low wind conditions (e.g., $U_{10} = 2.19 \text{ m s}^{-1}$), as well as the ability to detect a critical height (where the phase-averaged airflow velocity matches the phase speed of the average wave, see the phase-averaging method below) as close as 0.4 mm to the air–water interface (Buckley and Veron 2016). In contrast, the seminal PIV airflow measurements of Reul et al. (1999) above mechanically generated waves were achieved no less than 1.5 mm above the water surface.

2.4 Laser-induced fluorescence measurements of wind wave properties

While the surface detection images mentioned above are useful to locate the surface within the PIV images, in most cases, they did not have a sufficiently large footprint to capture entire wavelengths of the surface waves and/or did not acquire with sufficient temporal resolution

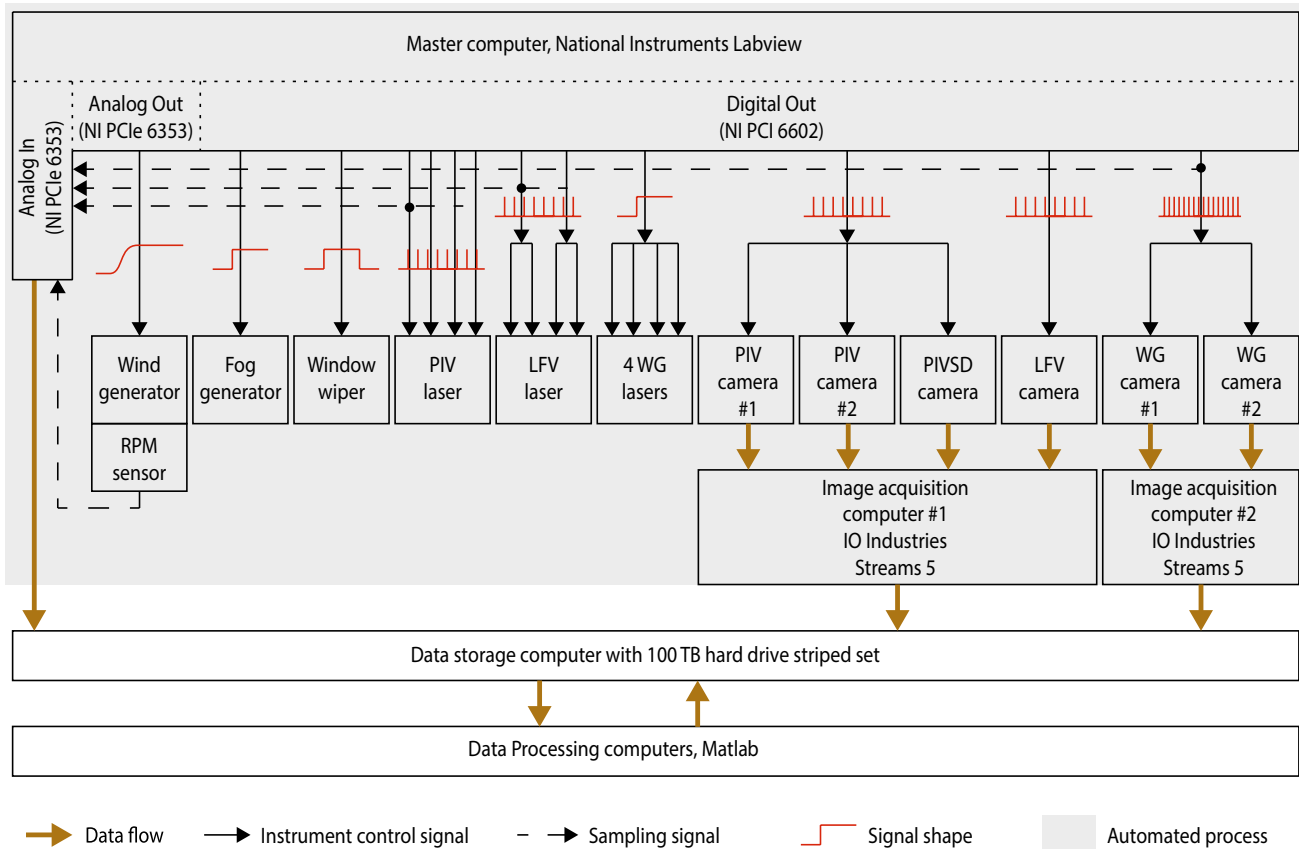


Fig. 3 Signal and data flow chart for the wind-wave experiments. The gray shaded area represents the event that we fully programmed and automated

to satisfactorily measure the wave frequency spectrum. This experimental setup, is, to the best of our knowledge, the first of its kind to combine PIV measurements with a large spatial LIF snapshots of the water surface elevation. Indeed, since the footprint of PIV images is generally limited by a requirement of high resolution, past studies were only able to resolve small fractions of the sampled waves. Since the wave phase of a single point along the water surface depends upon the wavenumber spectral analysis of the water surface elevation, it is important to “look” as far as possible up and downwind of the PIV image footprint. To quantify the wave field, two types of wave data were collected during these experiments: along-wind spatial surface profiles with high spatial resolution $\eta(x)$, and single point high frequency wave height measurements $\eta_i(t)$. Large along-wind spatial profiles of the wavy surface were obtained by LIF, using a CCD camera (Jai TM4200CL, 2048 × 2048 pixels, noted “LFV” hereafter, as in “large field of view”—Fig. 1), focused on the intersection with the surface of a large green laser sheet, generated by another pulsed dual-head Nd-Yag laser (New Wave Research, 120 mJ/pulse, 3–5 ns pulse duration). The LFV laser sheet was slightly tilted, by an angle of $\leq 5^\circ$, to clear

the underlying PIV mirror (see Fig. 1, bottom right panel). This laser was pulsed 20 μs before the first flash of the PIV laser. The LFV camera was fitted with a wide angle (115°) lens (Rokinon, 14 mm) and an amber acrylic band-pass optical filter (Kentek, 566 nm). The resulting LFV images provided measurements of the along-wind surface elevation in the center line of the channel over a length of 51.2 cm (250 $\mu\text{m}/\text{pixel}$ resolution), and at a rate of 7.2 Hz. The LFV field of view was positioned in the same along-channel plane as the PIV images, and extended 16.7 cm upwind and 15.8 cm downwind of the PIV field of view (Fig. 2b). Using the same edge detection algorithm as for the PIVSD images, the uncertainty on the location of the water surface on the LFV images was estimated to be ± 0.5 mm. Duncan et al. (1999) for example, used a similar LIF technique to study the surface profiles of mechanically generated breaking waves.

In addition, a single point optical wave gauge system, noted “WG”, provided time series of the water height, respectively 1.4 and 2.8 cm upwind and 2.7 and 4.2 cm downwind of the PIV airflow velocity measurements. The system consisted of two CCD cameras (Jai CV-M2CL—300 × 1600 pixel), each of which was fitted with a telephoto

lens (Nikon, 60 mm) and an amber acrylic bandpass filter (Kentek, 566 nm). The cameras are shown in Fig. 1. Each WG camera imaged the intersection with the surface of two 200 mW continuous green laser beams (see Fig. 2b). The resulting LIF images provided measurements of the water height with a resolution of 66 $\mu\text{m}/\text{pixel}$, and at a frequency of 93.6 Hz.

2.5 Experimental procedure

The entire imaging system was automated and computer-controlled, using National Instruments software and hardware. The triggers to all 6 cameras, the 2 pulsed Nd-Yag lasers, the 4 WG lasers, and the window wipers, were timed by PCI 6602 timing boards (National Instruments), and generated through BNC-2121 (National Instruments) connector blocks (see Fig. 3 below).

The acquisition sequence is as follows: first, the LfV laser was flashed at $t = 0$ s. The corresponding image was acquired with the LfV camera. Since total darkness was achieved in the laboratory, the LfV camera CCD only detected light during the LfV laser flash, that lasted 3–5 ns. This provided crisp sharp snapshots of the air–water interface (see Fig. 2). The LfV LIF imaging system only acquired one LfV image per PIV image pair, every 1/7.2 s. Next, the PIV (and PIVSD) images were acquired. The first PIV laser flash occurred, 20 μs after the LfV images at $t = 20$ μs , yielding the first images of a PIV pair. Note here that the wavy water surface did not display any detectable displacements within this 20 μs time interval. (A “PIV pair” here, represents actually a total of 6 images, since 2 PIV pairs and 1 PIVSD pair are acquired). The second PIV laser flash took place after a time interval Δt . Once again, since there was no other light source than the 3–5 ns laser flash, the PIV particle images were extremely sharp and in focus (see again Fig. 2a), even though the full exposure of the second PIV frame was constrained by camera electronics and forced to 67 ms. The PIV time interval Δt was adjusted for each experimental wind speed, to achieve optimal particle displacement on the PIV images for velocity vector calculation and ranged from $\Delta t = 300$ μs down to $\Delta t = 50$ μs at the highest wind speed.

In the meantime, the four continuous WG laser beams were on continuously. These did not contaminate the PIV and PIVSD images, because the WG beams were outside of the PIV and PIVSD fields of view. They were equally undetectable on the LfV fields of view, because the LfV camera exposure time was too short to detect these low power laser beams on such a large field of view. The two WG cameras were simultaneously triggered at a frequency of 93.6 Hz. This particular frequency was chosen because it is an integer multiple ($\times 13$) of 7.2 Hz, the PIV pair frequency. This allowed us to acquire 13 WG samples between each LfV/

PIV/PIVSD measurements, with no drift in the time intervals between LfV/PIV/PIVSD and WG samples. In fact the WG exposure time was kept short (8 μs), to optimize the WG signal resolution, and also to avoid contamination of every 13th WG image by the LfV/PIV/PIVSD laser flashes. The entire LfV/PIV/PIVSD laser flash and camera exposure sequence took place between two consecutive WG image acquisitions.

Each wind-wave experiment followed a fully automated, repeatable procedure. A data flow chart is provided in Fig. 3. At first, the wind was slowly increased to its target steady value. The wind blower was controlled by analog signals, generated and sampled by a PCIe 6353 data acquisition board (National Instruments) coupled with a BNC-2090A connector block (National Instruments). After the wave field had sufficiently developed and reached a fetch-limited equilibrium state, the fog generator was digitally triggered (see Fig. 3) and the system acquired simultaneously PIV data, LIF PIV surface detection data, LIF large field of view data, and LIF single point wave height data. During each experiment, the inside of the tank windows was dried using the window wipers every 30 s, and for a period of 3 s. The images altered by the presence of the wiper were later systematically removed from the dataset. During the acquisition, images were transferred to hard drive striped sets by IO Industries frame grabbers. The images were then accessed through Streams 5 software (IO Industries), and stored on a large data storage striped set after acquisition had ended. The data were later processed for image distortion correction, surface detection, and PIV velocity calculation using routines executed in Matlab.

2.6 Experimental conditions

For this study, wind speeds were generated ranging from 0.86 to 16.63 m s^{-1} (10-m extrapolated values, see Table 2). The peak wave phase celerity C_p and wave length λ_p were estimated using the linear deep-water dispersion relationship. The wave amplitudes a_p were computed as $a_p = \sqrt{2}a_{rms}$, where the rms surface elevation a_{rms} was obtained from the single point optical WG measurements. Overall, we studied 6 different wind speeds. Note that the lowest wind speed of 0.86 m s^{-1} did not generate any detectable surface waves.

Each of the experiments were performed for durations varying from 4.5 to 14 minutes, depending on the wind-wave conditions. Those durations were chosen based on the estimated dominant wavelength and wave speed for each experiment, with the objective of sampling the same number of waves (approximately 2000) for each condition. This resulted in a total number of images acquired by the imaging system ranging from 85,000 to 200,000, depending on the wind-wave conditions. The results presented in this study

were produced from the acquisition and processing of a total of over 1.9 Million images.

3 Results and discussion

3.1 Instantaneous 2D fields

Direct outputs of the PIV processing described above are shown in Fig. 4. Here, we show u , the horizontal component of the airflow velocity vector \mathbf{u} collected over wind waves for wind speeds of U_{10} ranging from 2.19 to 16.63 m s^{-1} (U_{10} is the wind speed extrapolated to a height of 10-m above the mean water level, a common practice in ocean science). These instantaneous horizontal velocity fields shown are not “best picks”; they were chosen because they give a representative picture of the dynamics upwind and downwind of crests, above waves at the peak of the spectrum. At the $U_{10} = 0.86 \text{ m s}^{-1}$ wind speed (not shown here), wind waves are not detected and the overall airflow resembles that over a solid flat plate. At higher wind speeds, the presence of waves significantly alters the airflow. In particular, for winds $U_{10} \geq 5.00 \text{ m s}^{-1}$, large wakes in the lee of the waves are clearly visible and suggest airflow separation. However, airflow separation from the surface cannot be assessed from velocity measurements alone which are not Galilean invariant. A more robust way to evaluate the occurrence of airflow separation events is through the visualization of kinematic fields obtained from the gradient velocity tensor $\nabla \mathbf{u}$ (Simpson 1989).

In Fig. 5, we show instantaneous kinematic fields in the airflow for a wind speed of $U_{10} = 5.00 \text{ m s}^{-1}$. The wave shown has a slope of $ak = 0.29$, where a and k are respectively the amplitude and dominant wavenumber of the wave, measured directly on the LFV image (see Fig. 6). This relatively steep wave has a sharp crest and a flat trough, as well as what appear to be parasitic capillary waves just downwind of the crest (e.g., Longuet-Higgins 1963; Phillips 1981; Ebu-chi et al. 1987; Perlin et al. 1993). In Fig. 5, the axes have been normalized with the peak wavenumber $k_p = 2\pi/\lambda_p$, velocities are normalized using the 10-m equivalent velocity U_{10} , and kinematic fields involving components of $\nabla \mathbf{u}$ are normalized using u_*^2/ν , i.e. the ratio of the friction velocity squared to the kinematic viscosity of air.² Above the crest of this steep wave, the airflow moves very fast throughout the entire height of the sampled air column, and the streamwise velocity decreases only very near the surface (Fig. 5a). This suggests that, over the crest, the viscous boundary layer is very thin, and the near surface shear is large. In aerodynamics, boundary layer thinning is known to occur in a similar

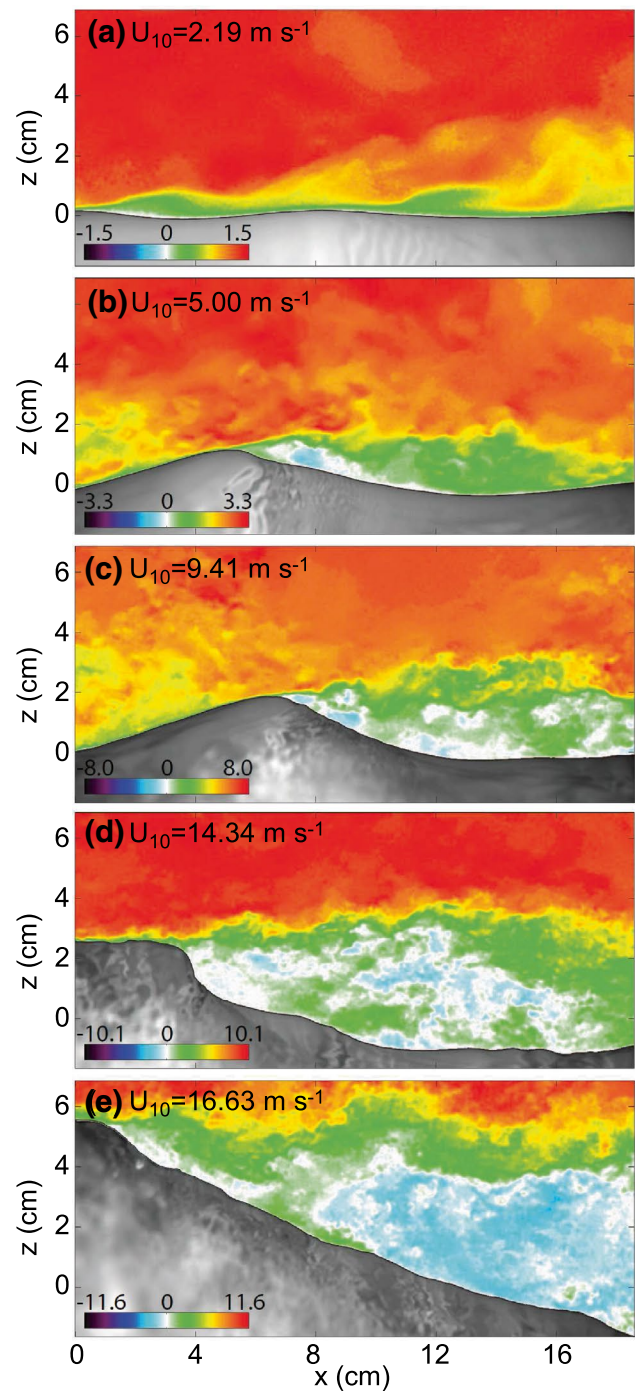


Fig. 4 Instantaneous horizontal velocity fields over wind waves with U_{10} ranging from 2.19 to 16.63 m s^{-1} . The color shows the horizontal velocity u in m s^{-1}

fashion in favorable pressure gradient conditions, on the leading edge of an airplane wing or the upwind side of a hill for example (Baskaran et al. 1987; Simpson 1989). Just past the wave crest, the shear layer appears to detach from the water surface, and the near surface streamwise velocity

² This normalization is equivalent to classical “wall layer” scaling.

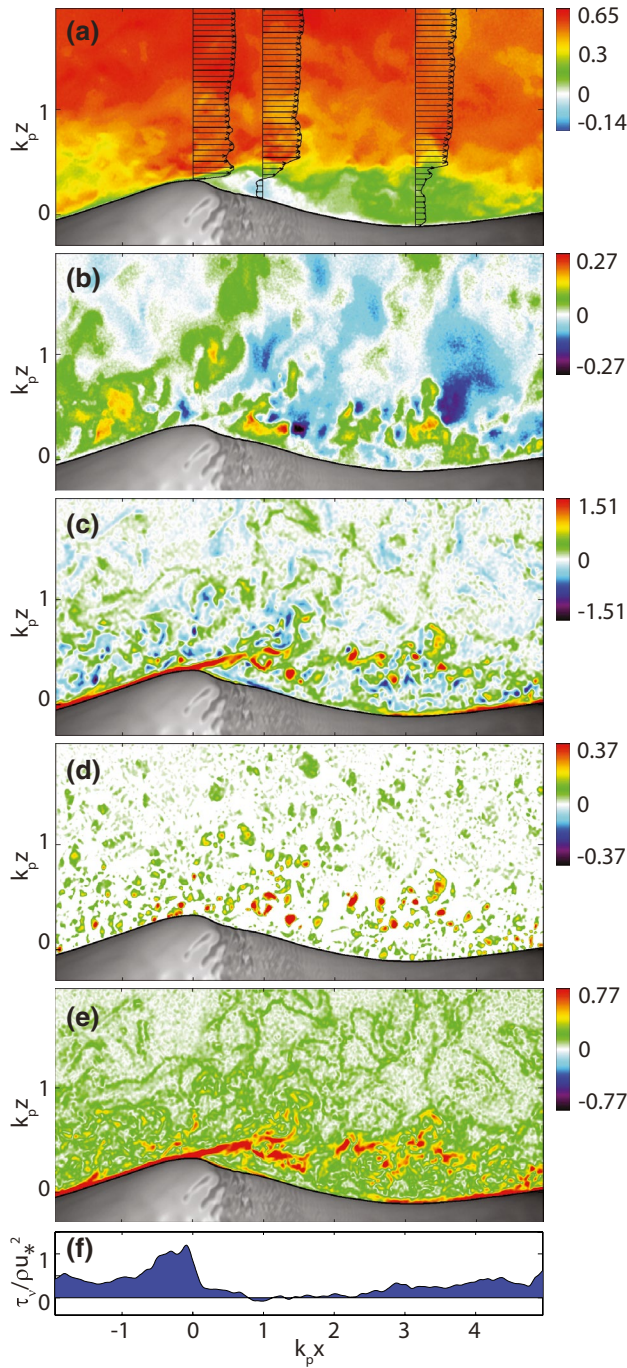


Fig. 5 Instantaneous fields over a wind wave, with $U_{10} = 5.00 \text{ m s}^{-1}$. **a** Horizontal velocity component u/U_{10} ; **b** Vertical velocity component w/U_{10} ; **c** Spanwise vorticity $\omega/(u_*^2/\nu)$; **d** Swirling strength $\lambda_{ci}/(u_*^2/\nu)$; **e** Shearing strength $\gamma/(u_*^2/\nu)$; **f** Surface viscous stress $\tau_v/(\rho u_*^2)$ (averaged from 100 and to 500 μm above the air–water interface)

drops dramatically. We observe a region of negative velocity near $k_p x = 0.8$, which indicates that the crest of the wave is completely sheltering this region from the wind, and that the airflow reverses within the sheltered region. The

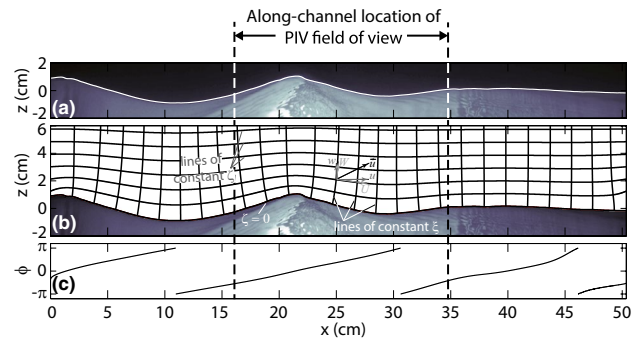


Fig. 6 **a** LFV image along with the instantaneous detected along-channel profile of the wavy water surface, with $U_{10} = 5.00 \text{ m s}^{-1}$. This profile, shown here in white, was obtained by applying our surface detection algorithm to the large field of view LIF image (LFV), shown here in grayscale. **b** Sketch of the surface following curvilinear coordinate system used in this study. The ζ coordinate is surface following at the surface, and decays toward the Cartesian coordinate z away from the surface. $\zeta = 0$ coincides with the water surface. The ξ coordinate is orthogonal to the surface at the surface, and decays toward the Cartesian coordinate x away from the surface. Measured variables u and w are respectively the horizontal and vertical components of the velocity \mathbf{u} in the (x, y) Cartesian coordinate system, and U and W are the corresponding velocity components in the (ξ, ζ) curvilinear coordinate system. **c** Along-surface wave phases obtained from a Hilbert transform of the surface profile

vertical velocity field w/U_{10} (Fig. 5b) shows that, upwind of the crest, the airflow is significantly forced upward near the surface. Downwind of the crest, near $k_p x = 0.8$, the airflow moves upward near the surface, then back downward near $k_p x = 1$ and continues to vary significantly above the wave trough (Fig. 5b). These variations are coherent with the separated sheltering hypothesis, which suggests the presence of recirculations past the point of separation (e.g., Simpson 1989). The spanwise vorticity field, plotted in Fig. 5c, confirms quite unequivocally the conjecture that the airflow is separating past the crest of the wave. The layer of high positive spanwise vorticity (mostly due to shear, see below), attached to the surface on the windward side of the wave, completely detaches from the surface past the crest of the wave. This (now free) high vorticity layer then appears to oscillate (near $k_p x = 0.8 - 1$), and break up into small centers of high (now essentially vortical, see below) vorticity. The oscillations of the unstable free shear layer past the wave crest are reminiscent of shear instabilities. The vortices that are shed past the crest show signs of vortex pairing or “roll-up” (for example just before $k_p x = 2$), similarly to those observed in perturbed free shear layers (e.g., Winant and Browand 1974; Ho and Huang 1982; Ho and Huerre 1984). We may also note here that there is no positive vorticity below the flow-reversed sheltered region, but rather slightly negative spanwise vorticity, which suggests flow reversal in that region.

To distinguish between eddies in the flow and vorticity that is shear-induced, we show estimates of the “swirling strength” λ_{ci} in Fig. 5d. The “swirling strength” is shown by Zhou et al. (1999) to be a measure of the strength of the local swirling motion. It is defined as the imaginary part of the complex eigenvalue of the velocity gradient tensor (Zhou et al. 1999). Here, in two dimensions, λ_{ci} is estimated as

$$\lambda_{ci} = \frac{1}{2} \text{Im} \left[\frac{\partial u}{\partial x} + \frac{\partial w}{\partial z} - \sqrt{\left(\frac{\partial u}{\partial x} - \frac{\partial w}{\partial z} \right)^2 + 4 \left(\frac{\partial u}{\partial z} \frac{\partial w}{\partial x} \right)} \right]. \tag{1}$$

We note that a number of other vortex identification criteria exists such as the Q-criterion (Hunt et al. 1988), the Δ -criterion (Chong et al. 1990), or the λ_2 -criterion (Jeong and Hussain 1995). These can be utilized as well but for the purpose of this paper, the details of the vortex identification method are not critical. Here, in Fig. 5d, we observe centers of intense positive spanwise swirling strength predominantly past $k_p x = 0.8$, which is where the detached high vorticity layer begins to lose coherence. This confirms that the observed centers of high vorticity (Fig. 5c) are due to eddies in the flow.

Conversely, to estimate the importance of shearing motions in the airflow, we decompose the velocity gradient tensor into a symmetrical part

$$S = \frac{1}{2} [\nabla \mathbf{u} + (\nabla \mathbf{u})^T], \tag{2}$$

and an anti-symmetrical part

$$\Omega = \frac{1}{2} [\nabla \mathbf{u} - (\nabla \mathbf{u})^T]. \tag{3}$$

The resulting tensors S and Ω are the strain rate tensor and rotation rate tensor respectively. The latter, also called vorticity tensor, contains only 3 distinct elements $\omega_i = -\epsilon_{ijk} \Omega_{jk}$, corresponding to the components of the vorticity vector $\boldsymbol{\Omega} = \nabla \times \mathbf{u}$. Thus S contains deformation of fluid elements other than solid body rotations. The deviatoric part of S , defined as:

$$\Gamma = S - \frac{1}{3} \text{tr}(S), \tag{4}$$

further contains the so-called “pure shear”, or deformations that are not associated with divergence in the flow since $\text{tr}(S) = \nabla \cdot \mathbf{u}$. In two dimensions, Γ contains two independent components and can, therefore, be represented by a vector $\boldsymbol{\Gamma}$. The “strength of anisotropic stretching”, or “shearing strength”, defined by Zhang et al. (2009) as the magnitude of $\boldsymbol{\Gamma}$ can then be expressed as:

$$\gamma = |\boldsymbol{\Gamma}| = \frac{1}{2} \sqrt{\left(\frac{\partial u}{\partial x} - \frac{\partial w}{\partial z} \right)^2 + \left(\frac{\partial u}{\partial z} + \frac{\partial w}{\partial x} \right)^2}. \tag{5}$$

In Fig. 5e, we have plotted γ corresponding to the velocity field of Fig. 5a, b. A thin layer of high γ , is present along the windward face of the wave, detaches from the crest, and extends up to $k_p x = 0.8$. The existence of this high γ layer, combined with the absence of significant swirling strength along that layer, suggests that the vorticity is essentially shear related, at least until the vortical layer becomes unstable and dislocates. Past $k_p x = 1$, downwind of the now disintegrated free shear layer, a number of vortices and small high shear structures occupy the turbulent boundary layer. Then, just before $k_p x = 3$, a high shear layer is gradually regenerated at the surface, indicating a progressive restoration of the surface-attached airflow.

In panel Fig. 5f we show along-wave surface viscous stress measurements, taken within the airflow’s viscous sub-layer (averaged from 100 and to 500 μm above the air–water interface). It can be noted that viscous stress is also commonly referred to as skin friction drag, in aerodynamics, (e.g. Schlichting and Gersten 2000). The viscous stress is computed from Eq. 9 below. Over the steeper, airflow separating wave, the viscous stress peaks at the crest, where it matches the total stress. It dramatically drops just past the crest, at the point of separation of the airflow. The surface viscous stress then becomes negative (below the flow reversal region), and remains close to zero up to $k_p x = 3$, and then slowly increases back up to $\approx 50\%$ of the total stress, on the windward side of the next downwind wave. These stress measurements compare very well with the measurements of Banner and Peirson (1998) (made on the waterside) and the measurements of Grare et al. (2013b)

3.2 Instantaneous 2D turbulent fields

To further the analysis of instantaneous data such as those presented above and to extract the turbulence, temporal or spatial averaging is generally required. Below, we present a triple decomposition (Phillips 1977) which splits kinematic fields into the sum of spatial mean, wave coherent, and turbulent components. This triple decomposition relies on proper phase detection and the use of a surface following coordinate system. In the following section, we show how our experimental design makes this analysis possible.

3.2.1 Coordinate transformation

In the top panel of Fig. 6, we display an example of an instantaneous LFV wave profile extracted from the wind wave experiment with $U_{10} = 5.00 \text{ m s}^{-1}$. Using the LFV wave profiles, we are able to decompose the water surface elevation $\eta(x)$ into spatial Fourier components:

$$\eta(x) = \sum_n a_n e^{i(k_n x + \phi_n)}. \tag{6}$$

where a_n , k_n and ϕ_n are respectively the amplitude, wavenumber, and phase of the n^{th} mode in the Fourier decomposition. From there, we derive an orthogonal curvilinear coordinate system $\Xi = (\xi, \zeta)$ that follows the surface near the surface, and tends toward the Cartesian $\mathbf{x} = (x, z)$ coordinate system away from the surface:

$$\xi(x, z) = x - i \sum_n a_n e^{i(k_n x + \phi_n)} e^{-k_n \zeta}, \quad (7)$$

$$\zeta(x, z) = z - \sum_n a_n e^{i(k_n x + \phi_n)} e^{-k_n \zeta}. \quad (8)$$

The rate at which the curvilinear system converges toward the Cartesian system is proportional to the wavenumber k_n of each wave mode. Since wind waves contain a number of different Fourier modes, the lines of constant ζ also contain several modes. Higher order modes (large wavenumbers) decay much faster than lower order modes. So, close to the surface, the curvilinear coordinate follows the wavy surface accounting for the small scale spatial variability. Away from the surface, only the influence of the longer waves will be accounted for. This is physically intuitive and it is similar to how wave orbital velocities behave. Here, this coordinate system simply accounts for the fact that longer waves influence the airflow up to a higher altitude than shorter waves do.

Figure 6b shows a sketch of the decaying surface-following grid. For clarity, only a small fraction of the grid lines is represented. Note that as we move away from the surface, high order modes such as the ripples present at the surface (grid line $\zeta = 0$) decay and disappear first, then the dominant mode decays slowly with height and the ζ -lines gradually tend toward the horizontal. The line $\zeta = 0$ corresponds exactly to the surface, and there, ξ is perpendicular to the surface. In other words, at the surface, the tangential component of the stress vector, for example, is readily obtained from

$$\tau_v = \rho v \left(\frac{\partial U}{\partial \zeta} + \frac{\partial W}{\partial \xi} \right), \quad (9)$$

where ρ is the air density and U and W are the velocity components projected in the ξ and ζ directions (Fig. 6b). A similar multi-modal curvilinear transformation was first used for a wind-wave interaction numerical model by Chalikov (1978), and more recently by Hara and Sullivan (2015). We note here that experimental results were, up until now, not reported using such coordinate systems.

3.2.2 Wave phase detection

Wave phase detection within the PIV field of view was achieved for wind waves by applying a Hilbert transform (Melville 1983; Oppenheim and Schaffer 2010) directly to the LFV wave elevation profiles. In Fig. 6c, the corresponding phases computed by Hilbert transform are plotted. Using this method, it is apparent that at the upwind and downwind extremities of the LFV wave profile, edge effects (unavoidable in discrete Fourier analysis) render the phase information unreliable. In fact, the curvilinear coordinate system suffers from similar edge effects also at the edges of the LFV wave profile, away from the PIV imaging area (see Fig. 6b). However, the phases and Fourier modes of the wavy surface located within the PIV field of view are well resolved since they are far away from the edges of the LFV field of view. Thus, for each vertical profile of kinematic fields (obtained from the PIV analysis) above the surface, a corresponding wave phase ϕ can be obtained. These phases will be subsequently used to perform phase averages. Here, we define ϕ in the interval $[-\pi, \pi]$, from wave trough to wave trough, with increasing phase in the downwind direction and $\phi = 0$ at the crest. Also, prior to performing the Hilbert transform, the LFV wave elevation profile was low-pass filtered to eliminate parasitic and other gravity-capillary waves with large wavenumbers. This resulted in a relatively narrow-banded wave signal centered around the peak wavenumber k_p and thus allowed for the Hilbert transform to detect the phase of the dominant waves.

Overall, this complex imaging system is, to the best of our knowledge, the first of its kind, capable of simultaneously measuring velocities in the air, along with robust temporal and spatial wave properties. Previous wave follower studies (e.g., Hsu et al. 1981), beyond the limitations caused by the one-dimensionality of the measurements, were also confronted to wave follower response times, which generated uncertainty in their phase detection and in estimating the height of their measurements from the water surface. This also prevented experimentalists from getting measurements close enough to the water surface. Grare et al. (2013b) were able to obtain measurements very close to the water surface by plunging their probe into the water, but this forced them to reduce the accuracy of their probe, to not destroy it upon submersion. Finally, we may mention here the work of Siddiqui and Loewen (2010), who, in spite of an effort to determine the phases of wind waves by linear interpolations of phases between zero-crossings, crests, and troughs of the peak waves, were limited by the difficulty to accurately detect surfaces on PIV images because of secondary laser light reflections, and by the limited size of their PIV field of view. Our combination of PIV images with simultaneous LIF PIVSD

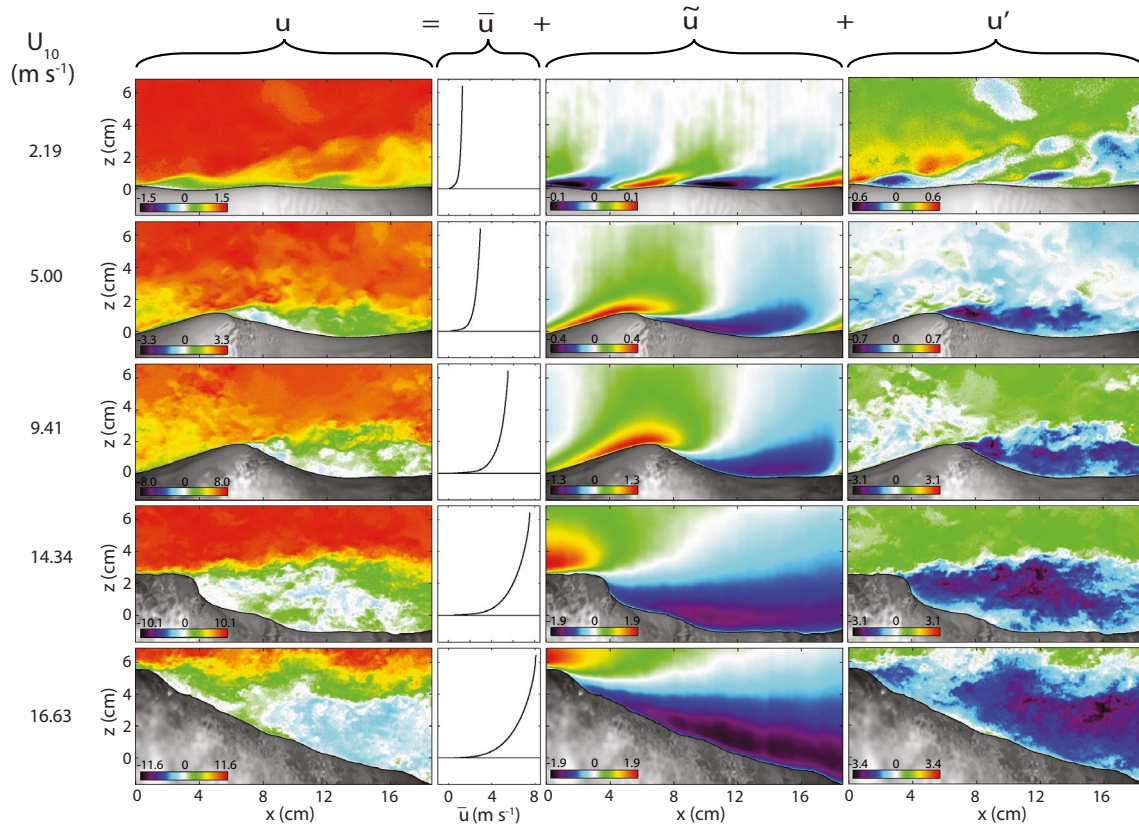


Fig. 7 Examples of triple decomposition (Eq. 11). The mean (\bar{u}), wave coherent (\tilde{u}), and turbulent (u') contributions to the instantaneous horizontal velocity fields u from Fig. 4, are shown. All quantities

are plotted in m s^{-1} . Each line corresponds to a different wind speed (in increasing order), with the wind speed written on the left of each line

and LFV images provided robust high resolution surface and wave phase detection for the air–water interface. The phase information was used to phase average the measured and computed quantities, and decompose them into ensemble mean, phase mean, and turbulent contributions.

3.2.3 Triple decomposition

The coordinate transformation and phase detection outlined above make it possible to assign a phase ϕ to any along-surface position ξ , and vice-versa (see Fig. 6c). In that sense, ϕ and ξ are interchangeable. Thus, instantaneous profiles (along ζ) of an instantaneous field $\mathbf{q}_i(\xi, \zeta)$ near the wavy interface, can be averaged together according to their phase ϕ . An intuitive way to think about this is that from the ensemble of all realizations of the profiles $\mathbf{q}_i(\zeta)$, available from all the data fields, we can construct a sub-ensemble $\mathbf{q}_s(\zeta)$ for a specific wave phase, say ϕ_0 . All the members of the ensemble can then be averaged together to yield the phase average at ϕ_0 . Repeating this procedure for different wave phases yields a phase mean denoted $\langle \mathbf{q} \rangle(\phi, \zeta)$ or equivalently $\langle \mathbf{q} \rangle(\xi, \zeta)$. Practically, the

sub-ensemble $\mathbf{q}_s(\zeta)$ is constructed from profiles for which the wave phase is within a bin $\phi_0 \pm \delta\phi$. The size of the bin is chosen to optimize phase resolution while also insuring that each sub-ensemble contains a sufficient number of distinct realizations to provide convergence of the phase averages.

Then, any instance of the field \mathbf{q}_i can be decomposed in the sum of a phase average and a turbulent perturbation (e.g., Hussain and Reynolds 1970; Phillips 1977):

$$\mathbf{q}_i(\xi, \zeta) = \langle \mathbf{q} \rangle(\xi, \zeta) + \mathbf{q}'_i(\xi, \zeta). \tag{10}$$

Turbulent quantities are, therefore, obtained by subtracting $\langle \mathbf{q} \rangle(\phi, \zeta)$ from instantaneous profiles $\mathbf{q}_i(\phi, \zeta)$.

The phase averaged quantity $\langle \mathbf{q} \rangle$ can be further decomposed into the sum of an ensemble mean (or average of all phases) $\bar{\mathbf{q}}$ and a wave-coherent deviation $\tilde{\mathbf{q}}$. This leads to the following triple decomposition:

$$\mathbf{q}_i(\xi, \zeta) = \bar{\mathbf{q}}(\zeta) + \tilde{\mathbf{q}}(\xi, \zeta) + \mathbf{q}'_i(\xi, \zeta). \tag{11}$$

We note that to define $\bar{\mathbf{q}}$ near the wavy boundary, it is in fact necessary to use a wave-following coordinate system, such as the one defined in Sect. 3.2.1. Otherwise, $\mathbf{q}(z)$ at a fixed

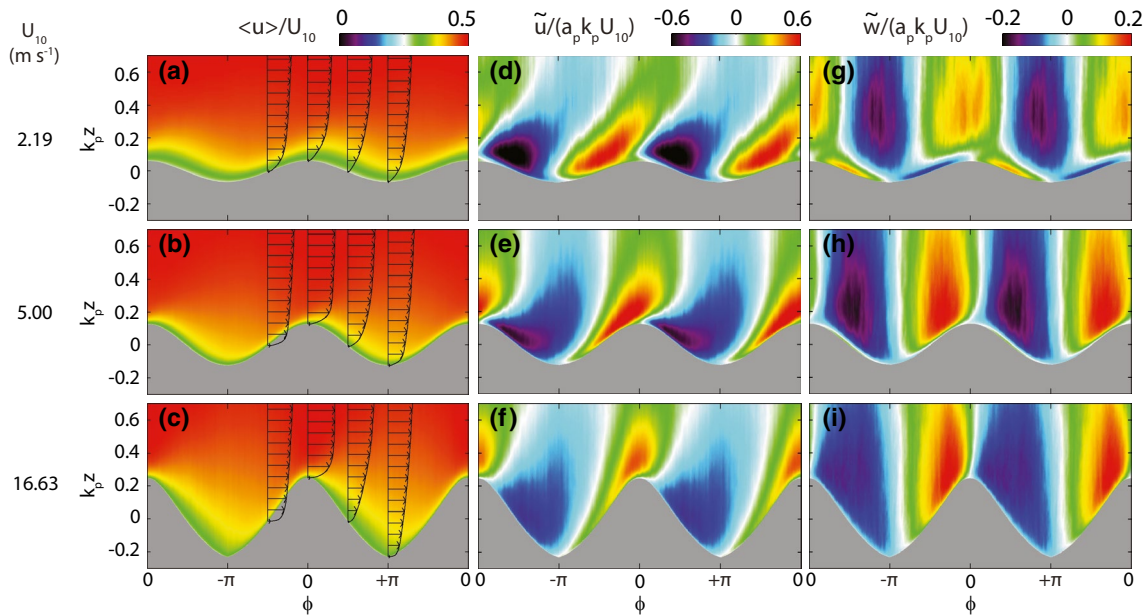


Fig. 8 Normalized phase averaged velocities, plotted over the mean water surface elevation. On the left, we show the horizontal velocity component $\langle u \rangle / U_{10}$, along with mean horizontal velocity pro-

files at wave phases $\phi = -\pi/2, 0, \pi/2, \text{ and } \pi$. The middle and right columns show respectively the horizontal $\tilde{u} / (a_p k_p U_{10})$ and vertical $\tilde{w} / (a_p k_p U_{10})$ components of the wave-induced perturbations

height z less than the wave amplitude, is alternatively in the air and in the water.

Equation 11 is illustrated in Fig. 7, where the instantaneous horizontal velocity fields previously shown in Fig. 4 are decomposed into the sum of a mean velocity profile, a wave-coherent, and a turbulent velocity field. The wave perturbation velocities \tilde{u} , which are wave phase coherent values, are plotted here over the instantaneous wave profiles. The turbulent fields u' are then computed by subtracting both the \tilde{u} fields and \bar{u} profiles, from instantaneous fields u . In this study, wind wave phases were separated into 144 distinct phase bins, each covering a phase interval of 4.36×10^{-2} rad.

3.3 Phase averaged data products

From here, we can compute phase or ensemble averages of a number of data products derived from wave-coherent or turbulent fields. For example, Fig. 8 shows normalized phase averaged velocities, plotted over the phase averaged water surface elevation for wind speeds U_{10} of 2.19, 5.00, and 16.63 m s^{-1} . The panels on the left show the horizontal velocity component $\langle u \rangle / U_{10}$, overlaid with phase averaged horizontal velocity profiles at wave phases $\phi = -\pi/2, 0, \pi/2, \text{ and } \pi$. For these slow and short wind waves, the airflow is faster on the upwind face of the waves than on the downwind face. This effect corresponds to a sheltering effect past the crest of the waves (Belcher and Hunt 1998) and leads to a thinning of the boundary layer as the airflow approaches

the crest, and a boundary layer thickening past the crest. This effect is particularly clear in the velocity profiles for $U_{10} = 16.63 \text{ m s}^{-1}$. In fact, the normalized wave-coherent horizontal velocity $\tilde{u} / (a_p k_p U_{10})$, shown in the middle panels (d, e, f) of Fig. 8, indeed indicate that the effect of waves is to accelerate the horizontal flow upwind of the surface waves, and decelerate the flow downwind of the waves. In addition, this effect is confined near the interface and decays exponentially away from the interface, as intuition would suggest, at a rate proportional to the surface wave peak wavenumber. The normalized wave-coherent vertical velocities $\tilde{w} / (a_p k_p U_{10})$ show common phase locked features: the air moves upward above positive wave slopes, and downward above negative slopes, a behavior that is expected and consistent with that of $\tilde{u} / (a_p k_p U_{10})$. At the lowest wind speed, however, within a thin layer near the surface, the behavior of $\tilde{w} / (a_p k_p U_{10})$ is reversed. The height of this reversal corresponds to the height of the so-called critical layer. At this height, the local wind speed matches that of the (dominant) surface wave. Below the critical layer the wind is slower than the surface wave and $\tilde{w} / (a_p k_p U_{10})$ is forced by wave orbital motion; above the critical layer, the wind is faster than the dominant wave which then acts in a similar way as a fixed obstacle would (see Buckley and Veron (2016) and references therein for details).

Additionally, Fig. 9 shows phase and ensemble averages of higher order data products such as wave and turbulent stresses for wind speeds U_{10} of 2.19, 5.00, and 16.63 m s^{-1} . The normalized phase averaged wave stress $\tilde{u}\tilde{w} / u_*^2$ (Fig. 9 panels a,

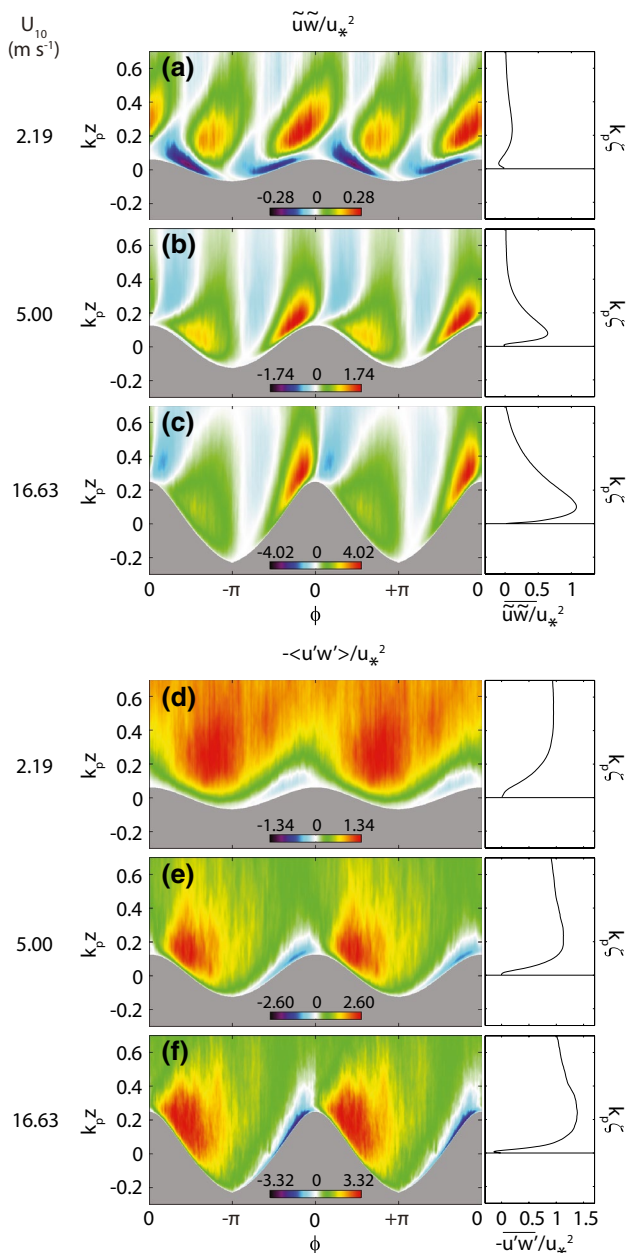


Fig. 9 Normalized phase averaged wave stress \widetilde{uw}/u_*^2 (first column) and total mean (across all phases) turbulent stress \widetilde{uw}/u_*^2 (second column). Normalized phase averaged turbulent stress $-\langle u'w' \rangle / u_*^2$ (third column) and total mean (across all phases) turbulent stress $-u'w' / u_*^2$ (last column). Phase averages are plotted above the phase averaged water surface elevation, and total mean profiles are plotted with respect to the surface following vertical coordinate ζ . Each line corresponds to one experiment, and the corresponding mean 10-m wind speeds are indicated on the left

b, and c) shows positive regions of intense wave stress along most of the upwind face of waves, as well as along most of the downwind face, where the positive stress is slightly less intense. These regions are interlaced with regions of negative

wave stress just downwind of crests (intense negative stress) and of troughs (less intense negative stress). The negative stress contours are pinched thin near the surface, such that the negative stress regions are barely connected to the surface, and they widen away from the surface. At the lowest wind speed, while the alternating positive-negative stress pattern exists in a broadly similar form away from the surface, near the surface the mean wave stress pattern is considerably different: the upwind and downwind faces of the wind waves are exposed to regions of negative wave stress, more intense downwind of crests, and slightly less intense upwind. In this case, the situation is almost exactly the mirror image of the higher wind speed cases. As in Fig. 8, this effect is confined below the critical layer height. Belcher and Hunt (1998) predicted this pattern and dubbed it “negative asymmetry” effect. On the right hand side of panels Fig. 9a–c, we show profiles of the normalized ensemble averaged wave stresses \widetilde{uw}/u_*^2 . As expected, the wave effects are confined near the interface. Note that these profiles are plotted with respect to the surface-following vertical coordinate ζ . Figures 9d–f show the normalized phase averaged turbulent stress $-\langle u'w' \rangle / u_*^2$. Regions of strong Reynolds stress are found on average downwind of the waves, which is where the boundary layer thickens. This phase-locked “jet” of increased turbulent stress can be related to the sheltering effect (separated or not) that occurs downwind of waves. The separation of the airflow past wave crests is the obvious candidate to explain increased turbulence production past crests since detached free shear layers and airflow separation are expected to produce substantial turbulence and vorticity (see Fig. 5c, d). The lowest wind speed here also differs in that the regions of high Reynolds stresses (downwind of crests) are only marginally more intense than the surrounding stresses at other phases. It is likely that these smaller slope waves do not cause as much separation as the others (Reul et al. 2008). We also note a near-surface layer of reduced turbulent stress at all phases. This suggests that within the critical layer, the work of turbulent forces on the waves is reduced.

Finally, to identify dominant motions in the airflow above waves, POD (proper orthogonal decomposition) can be applied to a set of velocity snapshots measured by PIV. POD analysis has been typically used to decompose flows in the vicinity of fixed boundaries (e.g., Palmer et al. 2012). In this paper, we describe a method of adapting the POD method to the airflow above moving surface waves, and we present some preliminary results for one low wind speed experiment ($U_{10} = 2.19 \text{ m s}^{-1}$, see results below). Briefly, the proper orthogonal decomposition of turbulent velocity fields \mathbf{u}' , consists in finding a basis of orthonormal spatial modes $\Psi_k(\mathbf{x})$, and temporal coefficients $a_k(t)$, such that:

$$\mathbf{u}'(\mathbf{x}, t) = \sum_k a_k(t) \Psi_k(\mathbf{x}). \tag{12}$$

To obtain the k th mode, the following eigenvalue problem needs to be solved:

$$\lambda_k \Psi_k(\mathbf{x}) = \int_{\mathcal{X}} \mathbf{R}(\mathbf{x}, \mathbf{y}) \Psi_k(\mathbf{y}) d\mathbf{y}, \tag{13}$$

where the two-point autocorrelation tensor is given by:

$$\mathbf{R}(\mathbf{x}, \mathbf{y}) = \int_{\mathcal{T}} \mathbf{u}'(\mathbf{x}, t) \otimes \mathbf{u}'(\mathbf{y}, t) dt, \tag{14}$$

and \mathcal{T} and \mathcal{X} represent time and physical spaces³ respectively. Orthonormality of the spatial modes requires that

$$\int_{\mathcal{X}} \Psi_k(\mathbf{x}) \Psi_l(\mathbf{x}) d\mathbf{x} = \delta_{kl}, \tag{15}$$

which in turn implies that the temporal coefficients are orthogonal and scaled such that:

$$\int_{\mathcal{T}} a_k(t) a_l(t) dt = \lambda_k \delta_{kl}. \tag{16}$$

The decomposition outlined above (Eq. 12) is particularly interesting because it leads to a convenient physical interpretation. Indeed, since the Reynolds stress tensor is a particular case of the autocorrelation tensor \mathbf{R} , each eigenvalue λ_k is proportional to the TKE content of the corresponding mode Ψ_k , and the sum of the eigenvalues $\sum_k \lambda_k$ is equivalent to twice the turbulent kinetic energy contained in the domain \mathcal{X} (see Luchtenburg et al. (2009) for details). In other words, the total TKE is:

$$TKE = \frac{1}{2} \sum_k \lambda_k. \tag{17}$$

Furthermore, modes with large eigenvalues represent the spatial patterns that contain a significant amount of TKE.

For the dataset presented here, as suggested by the instantaneous observations as well as the phase-averaged results presented thus far, the kinematics of the airflow above the waves strongly depend on the phase of the waves, as well as on the height above the water surface. Thus, we choose to perform a wave-phase dependent POD analysis. To do so, similarly to how we obtained phase averages, we construct an ensemble of instantaneous velocity profiles $\mathbf{u}'_s(\zeta)$ measured by PIV above the water surface at a wave phase ϕ_0 . Thus, the time domain \mathcal{T} consists of snapshots in time, and \mathcal{X} reduces to a single dimension along ζ . In that sense, as described above in Sect. 3.2.3, $\mathbf{u}'_s(\zeta)$ form a sub-ensemble of all available measurements $\mathbf{u}'_i(\xi, \zeta)$, at a location ξ along the interface where the wave phase is ϕ_0 .

Performing the snapshot POD analysis outlined above yields the spatial modes $\Psi_k(\mathbf{x}) = (\sigma_k, \theta_k)$, corresponding to

the turbulent velocity $\mathbf{u}'(\phi, \zeta)$. σ_k and θ_k are the horizontal and vertical components. σ_k and θ_k are the horizontal and vertical components of vector $\Psi_k(\mathbf{x})$ respectively. It can be noted that, following Eq. 12, both σ_k and θ_k represent energy resulting from both components (u' and w') of the velocity vector field. ‘‘Snapshot POD’’ was applied for example by Palmer et al. (2012) to PIV airflow measurements solid barchan dunes. Additional details on this technique were given by Sirovich (1987) and Cazemier et al. (1998). Here, we’ve adapted this method to the airflow over moving water surface waves, by defining a wave-dependent version of snapshot POD.

Figure 10 shows the 3 POD modes with the largest fractional TKE content, for the experiment with $U_{10} = 2.19$ m s⁻¹ (see panels a through f). For reference, the phase-averaged turbulent velocity variances and TKE for the same experiment are plotted on the right (panels g, h, i). Above $k_p \zeta \sim 0.2$, the first mode shows patterns consistent with a turbulent boundary layer over a flat wall: intense streamwise and downward turbulent motions. This mode also shows a slight intensification of streamwise motions above wave crests (see panel a). These effects are signs of the modulation of this boundary layer by the waves, otherwise known as non-separated sheltering. Interestingly, over these very small waves in low winds, it is mostly at the higher order modes (panels b and f for example), that we can see closed phase-locked contours downwind of crests, reminiscent of those in the turbulent stress (Fig. 9, panel d) and in the TKE components $\langle u'^2 \rangle / u_*^2$ and $\langle u'^2 + w'^2 \rangle / u_*^2$ (Fig. 10, panels g and i). These features are probably due to intermittent airflow separation events, which have been found to take place over a small percentage of the waves in these low wind conditions. Here, POD analysis allows to classify flow patterns in order of importance for the total TKE: In this low wind-speed experiment, turbulent flow patterns due to airflow separation events have a lower contribution to the total TKE than simple non-separated sheltering downwind of wave crests.

4 Conclusions

We have devised a multi-camera multi-laser system combining particle image velocimetry (PIV) and laser-induced fluorescence (LIF) to study the airflow over wind-driven surface waves. To the best of our knowledge, this system is the first of its kind, capable of simultaneously measuring the velocity in the airflow, along with robust spatial and temporal surface elevation properties. Spatial surface wave elevations over a large footprint afford the possibility of using Fourier techniques to define a multi-modal wave following coordinate system and determine the local phase of the peak surface waves. The PIV also estimates two-dimensional velocity fields above and within the viscous layer of the detected

³ In this general mathematical formulation, \mathcal{X} is $\mathcal{L}^2(\mathbb{R}^3)$.

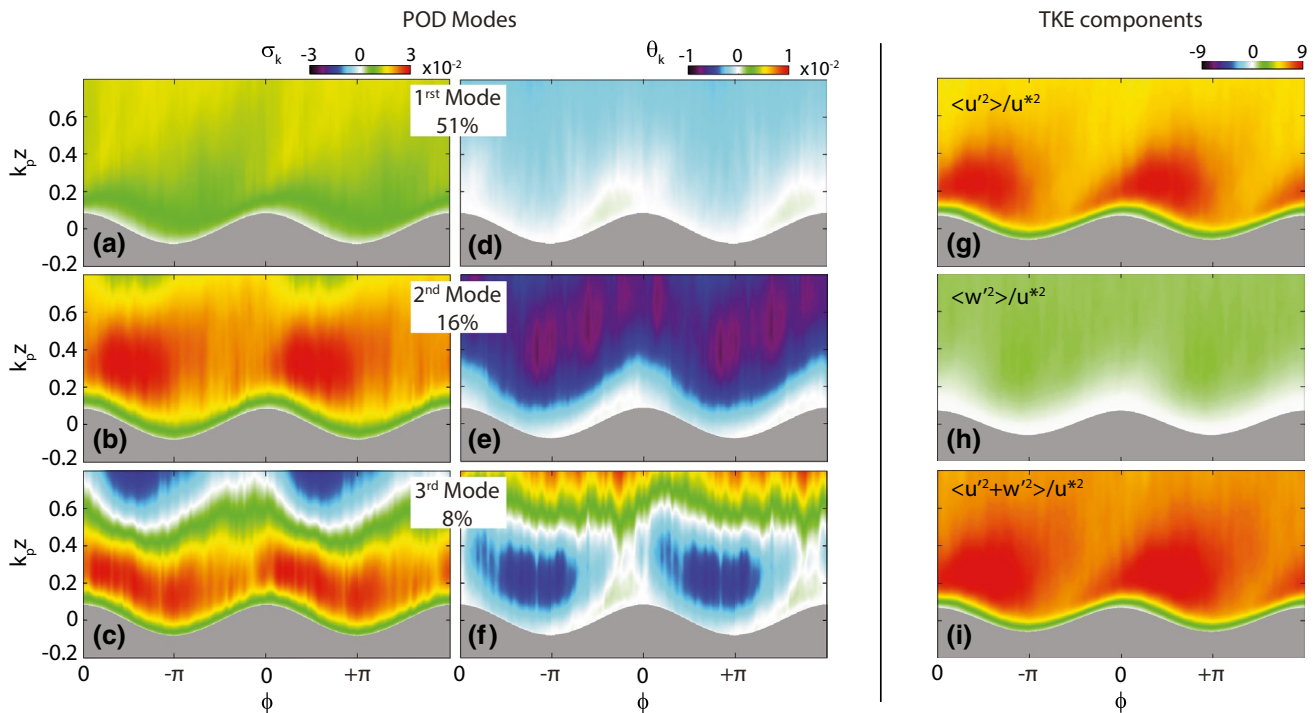


Fig. 10 a–f First 3 POD modes, and fractional TKE content of each mode averaged across all phases. Over 24000 velocity snapshots were used to compute the modes at each wave phase. g–i Normalized

phase-averaged turbulent variances $\langle u'^2 \rangle / u_*^2$ and $\langle w'^2 \rangle / u_*^2$ and TKE $\langle u'^2 + w'^2 \rangle / u_*^2$ for $U_{10} = 2.19 \text{ m s}^{-1}$

surface. Using the surface following coordinate system and the measured wave phases, meaningful ensemble and phase averages can be performed. These averages then allow for a triple decomposition whereby kinematic fields can be split in mean, wave-coherent, and turbulent components. Dynamically relevant phase or ensemble average data products can then be computed. Wave-phase dependent POD analysis provides promising insights into the structure of the turbulence over wind waves, and its coupling with the wave field. This paper is aimed at demonstrating the capability of the system, and we have thus shown only a subset of these data products. A thorough analysis of the kinematics and dynamics of the airflow over wind-generated waves will be the subject of subsequent publications. Finally, the techniques presented can be equally used for water-side measurements, which is encouraging for a possible use in simultaneous air–water measurements.

Acknowledgements This work was supported by US National Science Foundation grants OCE-1458977, OCE-1233808, OCE 0748767, and AGS-PRF-1524733

Open Access This article is distributed under the terms of the Creative Commons Attribution 4.0 International License (<http://creativecommons.org/licenses/by/4.0/>), which permits unrestricted use, distribution, and reproduction in any medium, provided you give

appropriate credit to the original author(s) and the source, provide a link to the Creative Commons license, and indicate if changes were made.

References

- Adrian R (1997) Dynamic ranges of velocity and spatial resolution of particle image velocimetry. *Meas Sci Technol* 8(12):1393
- Adrian RJ, Westerweel J (2011) Particle image velocimetry. Cambridge University Press, Cambridge, p 558
- Agrawal YC, Terray EA, Donelan MA, Hwang PA, Williams AJ III, Grennan WM, Kahma KK, Kitaigorodskii SA (1992) Enhanced dissipation of kinetic energy beneath surface waves. *Nature* 359:219–220
- André M, Bardet P (2014) Velocity field and surface profile resolution below steep and short surface waves. *Exp Fluids* 27:112103
- Anis A, Moum JN (1995) Surface wave-turbulence interactions: scaling $\epsilon(z)$ near the sea surface. *J Phys Oceanogr* 25:346–366
- Banner ML, Melville WK (1976) On the separation of air flow over water waves. *J Fluid Mech* 77:825–842
- Banner ML, Peirson WL (1998) Tangential stress beneath wind-driven air-water interfaces. *J Fluid Mech* 364:115–145
- Banner ML, Zappa CJ, Gemmrich JR (2014) A note on the Phillips spectral framework for ocean whitecaps. *J Phys Oceanogr* 44(7):1727–1734
- Baskaran V, Smits AJ, Joubert PN (1987) A turbulent flow over a curved hill part 1. growth of an internal boundary layer. *J Fluid Mech* 182:47–83. doi:10.1017/S0022112087002246

- Belcher SE, Hunt JCR (1993) Turbulent shear flow over slowly moving waves. *J Fluid Mech* 251:119–148
- Belcher SE, Hunt JCR (1998) Turbulent flow over hills and waves. *Annu Rev Fluid Mech* 30:507–538
- Belcher SE, Grant ALM, Hanley KE, Fox-Kemper B, Van Roekel L, Sullivan PP, Large WG, Brown A, Hines A, Calvert D, Rutgersson A, Pettersson H, Bidlot JR, Janssen PAEM, Polton JA (2012) A global perspective on langmuir turbulence in the ocean surface boundary layer. *Geophys Res Lett*. doi:[10.1029/2012GL052932](https://doi.org/10.1029/2012GL052932)
- Belden J, Techet AH (2011) Simultaneous quantitative flow measurement using piv on both sides of the air-water interface for breaking waves. *Exp Fluids* 50(1):149–161
- Buckley MP, Veron F (2016) Structure of the airflow above surface waves. *J Phys Oceanogr* 46(5):1377–1397
- Cazemier W, Verstappen R, Veldman A (1998) Proper orthogonal decomposition and low-dimensional models for driven cavity flows. *Phys Fluids* 10(7):1685–1699
- Chalikov DV (1978) The numerical simulation of wind-wave interaction. *J Fluid Mech* 87(3):561–582. http://journals.cambridge.org/abstract_S0022112078001767
- Chong MS, Perry AE, Cantwell BJ (1990) A general classification of three-dimensional flow fields. *Phys Fluids A* 2(5):765–777
- Cohn RK, Koochesfahani MM (2000) The accuracy of remapping irregularly spaced velocity data onto a regular grid and the computation of vorticity. *Exp fluids* 29(1):S061–S069
- D'Asaro EA (2014) Turbulence in the upper-ocean mixed layer. *Annu Rev Mar Sci* 6:101–115
- Donelan MA, Haus BK, Reul N, Plant WJ, Stiassnie M, Graber HC, Brown OB, Saltzman ES (2004) On the limiting aerodynamic roughness of the ocean in very strong winds. *Geophys Res Lett*. doi:[10.1029/2004GL019460](https://doi.org/10.1029/2004GL019460)
- Drazen DA, Melville WK (2009) Turbulence and mixing in unsteady breaking surface waves. *J Fluid Mech* 628:85–119. doi:[10.1017/S0022112009006120](https://doi.org/10.1017/S0022112009006120)
- Drennan WM, Donelan MA, Terray EA, Katsaros KB (1996) Oceanic turbulence dissipation measurements in swade. *J Phys Oceanogr* 26:808–815
- Duncan J, Qiao H, Philomin V, Wenz A (1999) Gentle spilling breakers: crest profile evolution. *J Fluid Mech* 379:191–222. http://journals.cambridge.org/abstract_S0022112098003152
- Ebuchi N, Kawamura H, Toba Y (1987) Fine structure of laboratory wind-wave surfaces studied using an optical method. *Bound-Layer Meteorol* 39(1–2):133–151
- Edson J, Fairall C (1998) Similarity relationships in the marine surface layer. *J Atmos Sci* 55:2311–2328
- Fouras A, Soria J (1998) Accuracy of out-of-plane vorticity measurements derived from in-plane velocity field data. *Exp Fluids* 25(5):409–430
- Gemmrich J, Farmer DM (2004) Near-surface turbulence in the presence of breaking waves. *J Phys Oceanogr* 34:1067–1086
- Gent PR, Taylor PA (1977) A note on separation over short wind waves. *Bound-Layer Meteorol* 11:65–87
- Grant AL, Belcher SE (2009) Characteristics of langmuir turbulence in the ocean mixed layer. *J Phys Oceanogr* 39:1871–1887
- Grare L (2009) Etude des interactions océan-atmosphère à proximité immédiate de l'interface: Application aux vagues de vent et aux vagues extrêmes. PhD thesis, University of Aix-Marseille
- Grare L, Lenain L, Melville WK (2013a) Wave-Coherent Airflow and Critical Layers over Ocean Waves. *J Phys Oceanogr* 43(10):2156–2172. doi:[10.1175/JPO-D-13-056.1](https://doi.org/10.1175/JPO-D-13-056.1), <http://journals.ametsoc.org/doi/abs/10.1175/JPO-D-13-056.1>
- Grare L, Peirson WL, Branger H, Walker JW, Giovanangeli JP, Makin V (2013b) Growth and dissipation of wind-forced, deep-water waves. *J Fluid Mech* 722:5–50, doi:[10.1017/jfm.2013.88](https://doi.org/10.1017/jfm.2013.88), http://journals.cambridge.org/abstract_S0022112013000888
- Hara T, Sullivan PP (2015) Wave boundary layer turbulence over surface waves in a strongly forced condition. *J Phys Oceanogr* 45:868–883. doi:[10.1175/JPO-D-14-0116.1](https://doi.org/10.1175/JPO-D-14-0116.1)
- Harcourt RR, D'Asaro EA (2008) Large-eddy simulation of langmuir turbulence in pure wind seas. *J Phys Oceanogr* 38:1542–1562
- Hare JE, Hara T, Edson JB, Wilczack JM (1997) A similarity analysis of the structure of airflow over surface waves. *J Phys Oceanogr* 27:1018–1037
- Hewitt G (2013) *Annular two-phase flow*. Elsevier, Oxford
- Ho CM, Huang LS (1982) Subharmonics and vortex merging in mixing layers. *J Fluid Mech* 119:443–473. doi:[10.1017/S0022112082001438](https://doi.org/10.1017/S0022112082001438)
- Ho CM, Huerre P (1984) Perturbed free shear layers. *Annu Rev Fluid Mech* 16(1):365–422
- Hristov T, Friehe CA, Miller S (1998) Wave coherent fields in the air flow over ocean waves: identification of cooperative behavior buried in turbulence. *Phys Rev Lett* 81:5245–5248
- Hsu C, Hsu E, Street R (1981) On the structure of turbulent flow over a progressive water wave: theory and experiment in a transformed, wave-following co-ordinate system. *J Fluid Mech* 105:87–117. http://journals.cambridge.org/abstract_S0022112081003121
- Hunt JC, Wray AA, Moin P (1988) Eddies, streams, and convergence zones in turbulent flows. Center for Turbulence Research Report CTR-S88
- Hussain AKMF, Reynolds WC (1970) The mechanics of an organized wave in turbulent shear flow. *J Fluid Mech* 41(2):241–258. http://journals.cambridge.org/abstract_S0022112070000605
- Janssen PAEM (1989) Wind induced stress and the drag of air flow over sea waves. *J Phys Oceanogr* 19(6):745–754
- Janssen PAEM (1999) On the effect of ocean waves on the kinetic energy balance and consequences for the inertial dissipation technique. *J Phys Oceanogr* 29:530–534
- Jeong J, Hussain F (1995) On the identification of a vortex. *J Fluid Mech* 285:69–94
- Kaimal JC, Finnigan JJ (1994) *Atmospheric boundary layer flows: their structure and measurement*. Oxford university press, Oxford
- Kimmoun O, Branger H (2007) A particle image velocimetry investigation on laboratory surf-zone breaking waves over a sloping beach. *J Fluid Mech* 588:353–397
- Komen GJ, Cavaleri M, Donelan M, Hasselmann K, Hasselmann S, Janssen PAEM (1994) *Dynamics and modeling of ocean waves*. Cambridge University Press, Cambridge
- Kudryavtsev V, Makin V (2002) Coupled dynamics of short waves and the airflow over long surface waves. *J Geophys Res*. doi:[10.1029/2001JC001251](https://doi.org/10.1029/2001JC001251)
- Kudryavtsev VN, Makin VK (2001) The impact of air-flow separation on the drag of the sea-surface. *Bound-Layer Meteorol* 98:155–171
- Kukulka T, Plueddemann AJ, Trowbridge JH, Sullivan PP (2010) Rapid mixed layer deepening by the combination of langmuir and shear instabilities - a case study. *J Phys Oceanogr* 40:2381–2400
- Li D, Katul GG, Bou-Zeid E (2015) Turbulent energy spectra and cospectra of momentum and heat fluxes in the stable atmospheric surface layer. *Bound-Layer Meteorol* 157(1):1–21
- Li R, Garrett C, Skyllingstad E (2005) A regime diagram for classifying turbulent large eddies in the upper ocean. *Deep-Sea Res* 52:259–278
- Longuet-Higgins MS (1963) The generation of capillary waves by steep gravity waves. *J Fluid Mech* 16(01):138–159
- Luchtenburg D, Noack B, Schlegel M (2009) An introduction to the pod galerkin method for fluid flows with analytical examples and matlab source codes. Berlin Institute of Technology MB1, Muller-Breslau-Strabe 11

- Lumley JL, Terray EA (1983) Kinematics of turbulence convected by a random wave field. *J Phys Oceanogr* 13(11):2000–2007
- McWilliams JC, Sullivan PP, Moeng CH (1997) Langmuir turbulence in the ocean. *J Fluid Mech* 334:1–30
- Mei R (1996) Velocity fidelity of flow tracer particles. *Exp Fluids* 22(1):1–13
- Melville WK (1983) Wave modulation and breakdown. *J Fluid Mech* 128:489–506. http://journals.cambridge.org/abstract_S0022112083000579
- Melville WK (1994) Energy dissipation by breaking waves. *J Phys Oceanogr* 24:2041–2049
- Melville WK (1996) The role of surface-wave breaking in air-sea interaction. *Annu Rev Fluid Mech* 28:279–321
- Melville WK, Shear R, Veron F (1998) Laboratory measurements of the generation and evolution of langmuir circulations. *J Fluid Mech* 364:31–58
- Melville WK, Veron F, White CJ (2002) The velocity field under breaking waves: coherent structures and turbulence. *J Fluid Mech* 454:203–233
- Mueller JA, Veron F (2009) Nonlinear formulation of the bulk surface stress over breaking waves: feedback mechanisms from air-flow separation. *Bound-Layer Meteorol* 130(1):117–134. doi:10.1007/s10546-008-9334-6
- Noh Y, Min HS, Raasch S (2005) Large eddy simulation of the ocean mixed layer: the effects of wave breaking and langmuir circulation. *J Phys Oceanogr* 34:720–735
- Oppenheim AV, Schaffer RW (2010) Discrete-time signal processing. Pearson Higher Education, London
- Palmer JA, Mejia-Alvarez R, Best JL, Christensen KT (2012) Particle-image velocimetry measurements of flow over interacting barchan dunes. *Exp Fluids* 52(3):809–829
- Peirson WL (1997) Measurement of surface velocities and shears at a wavy air-water interface using particle image velocimetry. *Exp Fluids* 23:427–437. <http://link.springer.com/article/10.1007/s003480050131>
- Perlin M, Lin H, Ting CL (1993) On parasitic capillary waves generated by steep gravity waves: an experimental investigation with spatial and temporal measurements. *J Fluid Mech* 255:597–620
- Phillips O (1981) The dispersion of short wavelets in the presence of a dominant long wave. *J Fluid Mech* 107:465–485
- Phillips OM (1977) The dynamics of the upper ocean. Cambridge University Press, Cambridge
- Raffel M, Willert CE, Wereley S, Kompenhans J (2013) Particle image velocimetry: a practical guide. Springer, New York
- Rapp RJ, Melville WK (1990) Laboratory measurements of deep-water breaking waves. *Philos Trans R Soc Lond A331*:735–800
- Reul N, Branger H, Giovanangeli JP (1999) Air flow separation over unsteady breaking waves. *Phys Fluids* 11:1959–1961
- Reul N, Branger H, Giovanangeli JP (2008) Air flow structure over short-gravity breaking water waves. *Bound-Layer Meteorol* 126:477–505
- Schlichting H, Gersten K (2000) Boundary-layer theory. Springer, New York
- Schwendeman M, Thomson J, Gemmrich JR (2014) Wave breaking dissipation in a young wind sea. *J Phys Oceanogr* 44(1):104–127
- Siddiqui K, Loewen M (2010) Phase-averaged flow properties beneath microscale breaking waves. *Bound-layer Meteorol* 134:499–523. doi:10.1007/s10546-009-9447-6, <http://link.springer.com/article/10.1007/s10546-009-9447-6>
- Simpson RL (1989) Turbulent boundary layer separation. *Annu Rev Fluid Mech* 21:205–234
- Sirovich L (1987) Turbulence and the dynamics of coherent structures part i: coherent structures. *Q Appl Math* 45(3):561–571
- Skyllingstad ED, Denbo DW (1995) An ocean large-eddy simulation of langmuir circulations and convection in the surface mixed layer. *J Geophys Res* 100:8501–8522
- Spedding G, Rignot E (1993) Performance analysis and application of grid interpolation techniques for fluid flows. *Exp Fluids* 15(6):417–430
- Sullivan PP, McWilliams JC (2002) Turbulent flow over water waves in the presence of stratification. *Phys Fluids* 14(3):1182–1195
- Sullivan PP, McWilliams JC (2010) Dynamics of winds and currents coupled to surface waves. *Annu Rev Fluid Mech* 42:19–42
- Sullivan PP, Edson JB, Hristov T, McWilliams JC (2008) Large-eddy simulations and observations of atmospheric marine boundary layers above nonequilibrium surface waves. *J Atmos Sci* 65:1225–1245. doi:10.1175/2007JAS2427.1
- Sutherland P, Melville WK (2013) Field measurements and scaling of ocean surface wave-breaking statistics. *Geophys Res Lett* 40(12):3074–3079
- Sutherland P, Melville WK (2015) Field measurements of surface and near-surface turbulence in the presence of breaking waves. *J Phys Oceanogr* 45(4):943–965
- Suzuki N, Hara T, Sullivan PP (2013) Impact of breaking wave form drag on near-surface turbulence and drag coefficient over young seas at high winds. *J Phys Oceanogr* 43(2):324–343, doi:10.1175/JPO-D-12-0127.1, <http://journals.ametsoc.org/doi/abs/10.1175/JPO-D-12-0127.1>
- Terray EA, Donelan MA, Agrawal YC, Drennan WM, Kahama KK, Williams AJ III, Hwang PA, Kitaigorodskii SA (1996) Estimates of kinetic energy dissipation under breaking waves. *J Phys Oceanogr* 26:792–807
- Thais L, Magnaudet J (1996) Turbulent structure beneath surface gravity waves sheared by the wind. *J Fluid Mech* 328:313–344
- Thomas M, Misra S, Kambhamettu C, Kirby JT (2005) A robust motion estimation algorithm for PIV. *Meas Sci Technol* 16(3):865–877. doi: 10.1088/0957-0233/16/3/031, <http://stacks.iop.org/0957-0233/16/i=3/a=031?key=crossref.939fedf4eca6146ee1bfef5c5ec25740>
- Thomson J, Schwendeman MS, Zippel SF, Moghimi S, Gemmrich J, Rogers WE (2016) Wave-breaking turbulence in the ocean surface layer. *J Phys Oceanogr* 46(6):1857–1870
- Thorpe SA (1993) Energy loss by breaking waves. *J Phys Oceanogr* 23:2498–2502
- Thorpe SA, Osborn TR, Farmer DM, Vagle S (2003) Bubble clouds and langmuir circulation: observations and models. *J Phys Oceanogr* 33:2013–2031
- Tropea C, Yarin AL, Foss JF (2007) Springer handbook of experimental fluid mechanics. Springer, New York
- Turney D, Banerjee S (2008) Transport phenomena at interfaces between turbulent fluids. *AIChE J* 54(2):344–349
- Veron F, Melville WK (1999) Pulse-to-pulse coherent doppler measurements of waves and turbulence. *J Atmos Oceanic Technol* 16:1580–1597
- Veron F, Melville WK (2001) Experiments on the stability and transition of wind-driven water surfaces. *J Fluid Mech* 446:25–65
- Veron F, Saxena G, Misra SK (2007) Measurements of the viscous tangential stress in the airflow above wind waves. *Geophys Res Lett*. doi:10.1029/2007GL031242
- Veron F, Melville WK, Lenain L (2008) Wave-coherent air-sea heat flux. *J Phys Oceanogr* 38(4):788–802
- Veron F, Melville WK, Lenain L (2009) Measurements of ocean surface turbulence and wave-turbulence interactions. *J Phys Oceanogr* 39:2310–2323
- Winant CD, Browand FK (1974) Vortex pairing : the mechanism of turbulent mixing-layer growth at moderate reynolds number. *J Fluid Mech* 63:237–255. doi:10.1017/S0022112074001121
- Yang D, Shen L (2010) Direct-simulation-based study of turbulent flow over various waving boundaries. *J Fluid Mech* 650:131–180

- Zappa CJ, Banner ML, Morison RP, Brumer SE (2016) On the variation of the effective breaking strength in oceanic sea states a. *J Phys Oceanogr* 46(7):2049–2061
- Zhang E, Yeh H, Lin Z, Laramée RS (2009) Asymmetric tensor analysis for flow visualization. *IEEE Trans Vis Comput Graph* 15(1):106–122
- Zhou J, Adrian R, Balachandar S, Kendall T (1999) Mechanisms for generating coherent packets of hairpin vortices in channel flow. *J Fluid Mech* 387:353–396. http://journals.cambridge.org/abstract_S002211209900467X